https://doi.org/10.1016/j.ijheatmasstransfer.2018.06.026

MHD thermosolutal natural convection and entropy generation of Carreau fluid in a heated enclosure with two inner circular cold cylinders, using LBM

GH. R. Kefayati *, H. Tang

Department of Mechanical Engineering, The Hong Kong Polytechnic University, Kowloon, Hong Kong SAR, China

Abstract

In this paper, thermosolutal natural convection and entropy generation in a heated enclosure with two inner cold cylinders filled with a non-Newtonian Carreau fluid in the presence of a uniform magnetic field has been simulated by Lattice Boltzmann Method (LBM). This study has been conducted for certain pertinent parameters of Rayleigh number (Ra = 10^4 and 10^5), the Buoyancy ratio (N = -1, 0.1, 1), Hartmann number (Ha = 0, 15, 30, 60, and 90), power-law indexes (n = 0.2, 1, and 1.8). Results indicate that the rise of Rayleigh number enhances heat transfer for various studied parameters. The increase in power-law index provokes heat and mass transfer to drop gradually. However, the effect of power-law index on heat and mass transfer declines steadily as Hartmann number rises. The enhancement of Hartmann number causes heat and mass transfer to decline significantly. The augmentation of the buoyancy ratio number enhances heat and mass transfer. The augmentation of Rayleigh number enhances different entropy generations and declines the average Bejan number. The increase in the power-law index provokes various irreversibilities to drop significantly; although, the increase in Hartmann number decreases the influence of power-law index on different entropy generations. The enhancement of the buoyancy ratio causes the summation entropy generations to increase considerably. It was found that the total entropy generation declines as Hartmann augments.

Key words: Entropy, Carreau fluid, Natural convection, MHD, Mass transfer, LBM

* Corresponding author. Tel: +852 27667815.
Email addresses: gholamreza.kefayati@polyu.edu.hk) (GH. R. Kefayati), h.tang@polyu.edu.hk (H. Tang).

1 Introduction

Following the recent study by authors [1,2]; in which thermosolutal natural convection and entropy generation of Carreau fluids in a hot enclosure with an inner cold cylinder were analysed, the effect of a uniform magnetic field on heat and mass transfer as well as entropy generation of a Carreau fluid in the presence of two cylinders have been studied. Since, this investigation is the combinations of various elements, each part and previous studies are stated in following explanations.

Natural convection driven by buoyancy due to simultaneous temperature and concentration gradients is generally referred to as double diffusive or thermosolutal convection. Thermosolutal convection occurs in a wide variety of fields such as oceanography, astrophysics, geology and metallurgy. Over the past decades, studies on Newtonian double diffusive convection have been reflected by a number of publications [3–8]. However, in many cited fields, the applied fluids show a non-Newtonian manner. Some limited studies about thermosolutal convection of power-law fluids in a two and three dimensional enclosures have been studied [9–11].

Magnetohydrodynamics (MHD) is the study of the interaction between magnetic fields and moving, conducting fluids. Magnetic fields influence many natural and man-made flows [12]. They are routinely used in industry to heat, pump, stir and levitate liquid metals. There are three types of magnetic fields; a terrestrial magnetic field which is maintained by fluid motion in the earths core, a solar magnetic field, which generates sunspots and solar flares, and a galactic field which influences the formation of stars. When a constant current is injected into a fluid under the influence of a magnetic field, the resulting Lorentz force will, in general, produce motion. Electromagnetic pumps were one of the earliest applications of MHD, and were routinely used in various industries. Two dimensional MHD natural and mixed convection of Newtonian fluids in a cavity with different boundary conditions have been studied widely by researchers [13–35]. In these studies, as an electrically-conducting fluid moves with velocity $\mathbf{u}$ through an imposed magnetic field, their average motion gives rise to an electric current density. The applied magnetic effect is the inclusion of the Lorentz body force to the momentum equations.

$$\mathbf{F_m} = \mathbf{J} \times \mathbf{B} \tag{1.1}$$

According to Ohm's law, the electric current density $\mathbf{J}$ is as

$$\mathbf{J} = \sigma \left(\mathbf{E} + \mathbf{u} \times \mathbf{B} \right) \tag{1.2}$$

σ and $\mathbf{E}$ are the electrical conductivity of the fluid and the electric field strength; respectively.

Due to the uniform magnetic field flux, the irrotational electric field is formed inside the enclosure.

$$\boldsymbol{\nabla} \times \mathbf{B} = 0 \tag{1.3}$$

The electric field $\mathbf{E}$ can be expressed as the gradient of electrical potential Φ as follows:

$$\mathbf{E} = -\boldsymbol{\nabla}\Phi \tag{1.4}$$

The conservation of electric current $\mathbf{J}$ yields

$$\boldsymbol{\nabla} \cdot \mathbf{J} = 0 \tag{1.5}$$

So, from the Eq.1.2 we have

$$\boldsymbol{\nabla}^2\Phi = \boldsymbol{\nabla} \cdot (\mathbf{u} \times \mathbf{B}) \tag{1.6}$$

For a two-dimensional MHD flow, it is shown that

$$\boldsymbol{\nabla} \cdot (\mathbf{u} \times \mathbf{B}) = 0 \tag{1.7}$$

As a result

$$\boldsymbol{\nabla}^2\Phi = 0 \tag{1.8}$$

All walls of the enclosure are electrically insulated and the viscous no-slip boundary condition is applied on. In other words, the fluid is bounded by perfectly conducting walls that provide a resistance-free path from induced current. It follows that

$$\boldsymbol{\nabla}\Phi = 0 \tag{1.9}$$

and therefore the electric field vanishes everywhere in the cavity. Finally, the Lorentz force by the induced current and the magnetic field flux can be calculated without solving the electromagnetism inside the cavity, as follows:

$$\mathbf{F_m} = \sigma\,(\mathbf{u} \times \mathbf{B}) \times \mathbf{B} \tag{1.10}$$

A uniform magnetic field of $\mathbf{B} = \mathrm{B_x}\mathbf{i} + \mathrm{B_y}\mathbf{j}$ is imposed and it makes an angle of θ with the horizontal axis. The magnitude of the magnetic field and the angle are

$$B = \sqrt{{\mathrm{B_x}}^2 + {\mathrm{B_y}}^2} \qquad \theta = \tan^{-1}\left(\frac{\mathrm{B_x}}{\mathrm{B_y}}\right) \tag{1.11}$$

A magnetic field is applied on the melt during solidification process in injection molding in Magnesium Injection Molding. Moreover, as we know the dominant heat transfer process in injection molding is convection while the melt rheology shows a carreau model [36].

Generally, fluids are classified into two main groups: Newtonian and non-Newtonian fluids. In most fluids without memory, the main difference between Newtonian and non-Newtonian fluids is the relationship between the extra stress tensor ($\boldsymbol{\tau}$) and the first Rivlin-Ericksen tensor ($\mathbf{A_1}$). The constitutive equation of an incompressible Newtonian fluid is written in the following form:

$$\boldsymbol{\tau} = \eta \mathbf{A_1}\ , \qquad \mathbf{A_1} = \nabla \mathbf{u} + (\nabla \mathbf{u})^T \tag{1.12}$$

where η is the dynamic viscosity. Eq.(1.12) shows that the extra tensor has a linear relation with the rate of deformation tensor or the first Rivlin-Ericksen tensor. Carreau fluid is a special sub-class of non-Newtonian fluids in which follows the Carreau model [37]. This model was introduced in 1972 and has been applied extensively up to date. The constitutive equation of an incompressible Carreau fluids is as

$$\boldsymbol{\tau} = \eta(II(\mathbf{A_1}))\ \mathbf{A_1} \tag{1.13}$$

where

$$\eta(II(\mathbf{A_1})) = \eta_\infty + (\eta_0 - \eta_\infty)\ \left[1 + (\lambda\, II(\mathbf{A_1}))^2\right]^{(n-1)/2}\ , \quad II(\mathbf{A_1}) = \frac{1}{\sqrt{2}}\sqrt{\mathbf{A_1} : \mathbf{A_1}} \tag{1.14}$$

where $II(\mathbf{A_1})$ is the second Rivlin–Ericksen tensor. η_0 and η_∞ are the viscosities corresponding to zero and infinite viscosities, λ is the time constant and n is the power-law index where the deviation of n from unity indicates the

degree of deviation from Newtonian behavior. With n≠1, the constitute equation represents pseudoplastic fluid ($0 < n < 1$) and for ($n > 1$) it represents a dilatant fluid, respectively. Note that a Newtonian fluid can be recovered as a special case of the present Carreau fluid by letting n = 1 and/or $\lambda = 0$, and a power-law fluid can be obtained by assuming a large λ. The infinite shear viscosity, η_∞, is generally associated with a breakdown of the fluid, and is frequently significantly smaller ($10^3 - 10^4$ times smaller) than η_0. Carreau models have been employed to simulate various chemicals, molten plastics, slurries, paints, blood, etc.

Some limited isothermal and non-isotermal problems of Carreau fluids have been studied. Shamekhi and Sadeghy [38] analyzed lid-driven cavity flow of a purely-viscous non-Newtonian fluid obeying Carreau-Yasuda rheological model numerically using the PIM meshfree method combined with the Characteristic-Based Split-A algorithm. Results were reported for the velocity and pressure profiles at Reynolds numbers as high as 1000 for a non-Newtonian fluid obeying Carreau-Yasuda rheological model. The results showed a strong effect of the fluids non-Newtonian behavior, e.g. its shear-thinning behavior, on the velocity profiles inside an enclosure. In addition, it was demonstrated that the power-law index and time constant dramatically affected the size and the position of the primary vortex inside the cavity. Bouteraa et al. [39] performed a linear and weakly nonlinear analysis of convection in a layer of shear-thinning fluids between two horizontal plates heated from below. The shear-thinning behaviour of the fluid was described by the Carreau model. Analysis of the saturation coefficients at cubic order in the amplitude equations showed that the nature of the bifurcation depends on the rheological properties, i.e. the fluid characteristic time and shear-thinning index. For weakly shear-thinning fluids, the bifurcation was supercritical and the heat transfer coefficient increased, as compared with the Newtonian case. When the shear-thinning character was large enough, the bifurcation was subcritical, pointing out the destabilizing effect of the nonlinearities arising from the rheological law. It was shown that in the supercritical regime, only rolls were stable near onset. Pantokratoras [40] considered the flow of a non-Newtonian, Carreau fluid, directed normally to a horizontal, stationary, circular cylinder. The problem was investigated numerically using the commercial code ANSYS FLUENT with a very large calculation domain in order that the flow could be considered unbounded. It was found that for each Carreau number and each power-law index a critical Reynolds number exists where the wake appears. Below this critical Reynolds number no wake exists. They also mentioned all critical Reynolds numbers rise with increasing power-law index. For shear-thickening fluids the variation of critical Reynolds number is monotonic with Carreau number, that is, as the Carreau number increases that critical Reynolds number increases and the opposite is valid for shearthinning fluids. At low power-law index, the wake length changes non-linearly with increasing Reynolds number and as the power-law index rises the variation becomes linear. When the Carreau number became higher the drag coefficient of shear-thinning fluids decreased and

raised in shear-thickening fluids and this happened for all Reynolds numbers. Shahsavari and McKinley [41] studied the flow of generalized Newtonian fluids with a rate-dependent viscosity through fibrous media with a focus on developing relationships for evaluating the effective fluid mobility. They conducted a numerical solution of the Cauchy momentum equation with the Carreau or power-law constitutive equations for pressure-driven flow in a fiber bed consisting of a periodic array of cylindrical fibers. While the dimensionless mobility was, in general, a function of the Carreau number and the medium porosity, the results showed that for porosities less than $\epsilon \simeq 0.65$, the dimensionless mobility became independent of the Carreau number and the mobility function exhibited power-law characteristics as a result of the high shear rates at the pore scale. We derived a suitable criterion for determining the flow regime and the transition from a constant viscosity Newtonian responsed to a power-law regime in terms of a new Carreau number rescaled with a dimensionless function which incorporates the medium porosity and the arrangement of fibers.

Many studies have conducted the effect of the presence of isothermal bodies inside the enclosure on the natural convection phenomena and focused on the diverse body shapes, e.g. circular, square and triangular cylinders. Kim et al. [42] carried out numerical calculations for natural convection induced by a temperature difference between a cold outer square enclosure and a hot inner circular cylinder. They investigated the effect of the inner cylinder location on the heat transfer and fluid flow. Further, the location of the inner circular cylinder was changed vertically along the center-line of square enclosure. Mehrizi et al. [43] investigated a numerical study for steady-state, laminar natural convection in a horizontal annulus between a heated triangular inner cylinder and cold elliptical outer cylinder, using lattice Boltzmann method. Both inner and outer surfaces were maintained at the constant temperature and air was the working fluid. Park et al. [44] studied the natural convection induced by a temperature difference between a cold outer square enclosure and two hot inner circular cylinders. A two-dimensional solution for natural convection in an enclosure with inner cylinders was obtained using an accurate and efficient immersed boundary method. The immersed boundary method based on the finite volume method was used to handle inner cylinders located at different vertical centerline positions of the enclosure for different Rayleigh numbers. Mehrizi and Mohamad [45] utilized Lattice Boltzmann method to simulate steady-state, laminar, free convection in two-dimensional annuli between a heated triangular inner cylinder and elliptical outer cylinder. The study was performed for different inclination angles of inner triangular and outer elliptical cylinders. Seo et al. [46] conducted two-dimensional numerical simulations for the natural convection phenomena in a cold square enclosure with four hot inner circular cylinders. The immersed boundary method (IBM) was used to capture the virtual wall boundary of the four inner cylinders based on the finite volume method (FVM). Zhang et al. [47] investigated a numerical study for steady-state natural convection in a cold outer square

enclosure containing a hot inner elliptic cylinder using the variational multi-scale element free Galerkin method (VMEFG). In the cited studies, the fluids have been assumed to be Newtonian fluids while most materials demonstrates non-Newtonian behavior.

The optimal design of the cited industries is obtained with precision calculation of entropy generation since it clarifies energy losses in a system evidently. Entropy generation on natural convection has been scrutinized in some researches. Ilis et al. [48] investigated entropy generation in rectangular cavities with different aspect ratios numerically. It was demonstrated that heat transfer and fluid friction irreversibility in a cavity vary considerably with the studied aspect ratios. In addition, the total entropy generation in a cavity increases with Rayleigh number, however, the rate of increase depends on the aspect ratio. El-Maghlany et al. [49] analyzed entropy generation associated with laminar natural convection in an infinite square cavity, subjected to an isotropic heat field with various intensities for different Rayleigh numbers. Mun et al.[50] studied entropy generation of natural convection in square enclosure with an inner cylinder. They scrutinized the simulations for different Rayleigh numbers, inclined angles, and Prandtl numbers. Doo et al.[51] analyzed entropy generation of natural convection in square enclosure with inner cylinder. They scrutinized the simulations for different Rayleigh numbers, the vertical position of inner cylinder, and Prandtl numbers.

Lattice Boltzmann method (LBM) has been demonstrated to be a very effective mesoscopic numerical method to model a broad variety of complex fluid flow phenomena. In traditional CFD tools e.g. ANSYS or STAR-CCM+, Navier-stokes equations are solved by FVM/FEM while the main equations of LBM are hyperbolic and can be solved locally, explicitly, and efficiently on parallel computers. So, the computation process decreases immensely, and the running time drops considerably. However, the specific relation between the relaxation time and the viscosity has caused LBM not to have the considerable success in non-Newtonian fluid especially on energy equations. In this connection, Fu et al. [52] proposed a new equation for the equilibrium distribution function, modifying the LB model. Here, this equilibrium distribution function is altered in different directions and nodes while the relaxation time is fixed. Independency of the method to the relaxation time in contrast with common LBM provokes the method to solve different non-Newtonian fluid energy equations successfully as the method protects the positive points of LBM simultaneously. In addition, the validation of the method and its mesh independency demonstrates that is more capable than conventional LBM. Huilgol and Kefayati [53] derived the three dimensional equations of continuum mechanics for this method and demonstrated that the theoretical development can be applied to all fluids, whether they be Newtonian, or power law fluids, or viscoelastic and viscoplastic fluids. Following the study, Huilgol and Kefayati [54] developed this method for the cartesian, cylindrical and spherical

coordinates.

The main aim of this study is to simulate heat and mass transfer, fluid flow, entropy generation of double diffusive natural convection of Carreau fluid in a heated enclosure with two inner cold cylinders in the presence of a uniform magnetic field. The innovation of this paper is studying the effect of a magnetic field on the cited fluid flow and geometry. LBM has been employed to study the problem numerically. Moreover, it is endeavored to express the effects of different parameters on entropy generations. The obtained results are validated with previous numerical investigations and the effects of the main parameters are researched.

2 Theoretical formulation

The geometry of the present problem is shown in Fig.1. The temperature and concentration of the enclosure walls have been considered to be maintained at high temperature and concentration of T_H and C_H as the circular cylinders are kept at low temperature and concentration of T_C and C_C. The cylinders centres have been fixed at (x_{c1} = 0.5 L , y_{c1} = 0.3 L) and (x_{c2} = 0.5 L , y_{c2} = 0.7 L); respectively. The inner circular cylinders have the fixed radii at R_d = 0.1 L. There is no heat generation and thermal radiation. The flow is incompressible, and laminar. The density variation is approximated by the standard Boussinesq model for temperature and concentration. The viscous dissipation and joule heating terms in the energy equation have been analysed in this study. A uniform magnetic field with a constant magnitude is applied in different inclinations (θ) where the horizontal direction from the left to right sides is the inclined angle of $\theta = 0°$. For most industrial flows involving carreau fluids e.g. liquid metal, magnetic Reynolds number is very low, usually less than 10^{-2}. When an external magnetic field is present, it is customary at such low values of magnetic Reynolds number to make use an approximation. In this approximation, induced magnetic fluctuations are much smaller than the applied magnetic field. Therefore, the induced magnetic field is neglected. Moreover, Hall effect is assumed negligible.

2.1 Non-dimensional equations

We define the buoyancy velocity scale $U = \left(\frac{\alpha}{L}\right) \mathrm{Ra}^{0.5}$ as Ra is the Rayleigh number. In order to proceed to the numerical solution of the system, the following non dimensional variables are introduced [1,2].

$$t^* = \frac{t\,U}{L}, \quad x^* = x/L, \quad y^* = y/L, \quad \mathbf{u}^* = \frac{\mathbf{u}}{U}, \quad {p_d}^* = \frac{p_d}{\rho\,U^2}, \tag{2.1}$$

$$T^* = (T - T_C)/\Delta T, \quad \Delta T = T_H - T_C, \quad \boldsymbol{\tau}^* = \frac{\sqrt{2}\,\boldsymbol{\tau}\,L}{\eta\,U} \tag{2.2}$$

$$C = (\bar{C} - C_C)/\Delta C \quad \Delta C = C_H - C_C \tag{2.3}$$

By substitution of Eqs. (2.1) - (2.3), the following system of non-dimensional mass, momentum, energy, and concentration equations are derived

$$\frac{\partial u}{\partial x} + \frac{\partial v}{\partial y} = 0 \quad , \tag{2.4}$$

$$\begin{aligned} \frac{\partial u}{\partial t} + u\frac{\partial u}{\partial x} + v\frac{\partial u}{\partial y} = -\frac{\partial p_d}{\partial x} + \frac{\mathrm{Pr}}{\sqrt{\mathrm{Ra}}}\left(\frac{\partial \tau_{xx}}{\partial x} + \frac{\partial \tau_{xy}}{\partial y}\right) \\ + \frac{\mathrm{Pr\,Ha}^2}{\sqrt{\mathrm{Ra}}}\left(v\,sin\theta\,cos\theta - u\,sin^2\theta\right), \end{aligned} \tag{2.5}$$

$$\begin{aligned} \frac{\partial v}{\partial t} + u\frac{\partial v}{\partial x} + v\frac{\partial v}{\partial y} = -\frac{\partial p_d}{\partial y} + \frac{\mathrm{Pr}}{\sqrt{\mathrm{Ra}}}\left(\frac{\partial \tau_{xy}}{\partial x} + \frac{\partial \tau_{yy}}{\partial y}\right) + \mathrm{Pr}\,(T - \mathrm{N}\,C) \\ + \frac{\mathrm{Pr\,Ha}^2}{\sqrt{\mathrm{Ra}}}\left(u\,sin\theta\,cos\theta - v\,cos^2\theta\right), \end{aligned} \tag{2.6}$$

$$\begin{aligned} \frac{\partial T}{\partial t} + u\frac{\partial T}{\partial x} + v\frac{\partial T}{\partial y} = \frac{1}{\sqrt{\mathrm{Ra}}}\left(\frac{\partial^2 T}{\partial x^2} + \frac{\partial^2 T}{\partial y^2}\right) \\ + \frac{\mathrm{Pr\,Ec}}{\sqrt{\mathrm{Ra}}}\left[\tau_{xx}\left(\frac{\partial u}{\partial x}\right) + \tau_{xy}\left(\frac{\partial u}{\partial y} + \frac{\partial v}{\partial x}\right) + \tau_{yy}\left(\frac{\partial v}{\partial y}\right)\right] \\ + \frac{\mathrm{Pr\,Ec\,Ha}^2}{\sqrt{\mathrm{Ra}}}\left(u\,sin\theta\, - v\,cos\theta\right)^2, \end{aligned} \tag{2.7}$$

$$\frac{\partial C}{\partial t} + u\frac{\partial C}{\partial x} + v\frac{\partial C}{\partial y} = \frac{1}{\mathrm{Le}\sqrt{\mathrm{Ra}}}\left(\frac{\partial^2 C}{\partial x^2} + \frac{\partial^2 C}{\partial y^2}\right) \tag{2.8}$$

The non-dimensional apparent viscosity is given by [1,2]

$$\eta(II(\mathbf{A_1})) = \frac{\eta_\infty}{\eta_0} + (1 - \frac{\eta_\infty}{\eta_0}) \left[1 + (\text{Cu } II(\mathbf{A_1}))^2\right]^{(n-1)/2} \tag{2.9}$$

The ratio η_∞/η_0 has been fixed at 0.001.

$$II(\mathbf{A_1}) = \left\{ 2 \left[\left(\frac{\partial u}{\partial x}\right)^2 + \left(\frac{\partial v}{\partial y}\right)^2 \right] + \left(\frac{\partial v}{\partial x} + \frac{\partial u}{\partial y}\right)^2 \right\}^{\frac{1}{2}} \tag{2.10}$$

Hence, the stresses are:

$$\tau_{xx} = 2\eta(II(\mathbf{A_1})) \left(\frac{\partial u}{\partial x}\right) \quad \tau_{yy} = 2\eta(II(\mathbf{A_1})) \left(\frac{\partial v}{\partial y}\right) \quad \tau_{xy} = \eta(II(\mathbf{A_1})) \left(\frac{\partial u}{\partial y} + \frac{\partial v}{\partial x}\right) \tag{2.11}$$

The non-dimensional parameters and their physical meanings for the problem are as follows:

Rayleigh number (Ra): It is the buoyant force divided by the product of the viscous drag and the rate of heat diffusion. In addition, Rayleigh Number (Ra) is a quantitative measure or representation of when the switch from conductive to convective transport happens for a given fluid plus geometry configuration. Once the Ra exceeds a critical value, henceforth, the dominant energy transport mechanism in the fluid would be convection. Here, two Rayleigh numbers (Ra = 10^4 and 10^5); which belongs to convection process and laminar flow, have been selected to be studied.

$$\text{Ra} = \frac{\rho\, \beta_T\, g L^3 \Delta T}{\eta\, \alpha} \tag{2.12}$$

Prandtl number (Pr): It is representing the ratio of diffusion of momentum to diffusion of heat in a fluid. In heat transfer problems, the Prandtl number controls the relative thickness of the momentum and thermal boundary layers. When Pr is small, it means that the heat diffuses quickly compared to the velocity (momentum). This means that for liquid metals the thickness of the thermal boundary layer is much bigger than the velocity boundary layer. So, here, Prandtl number is fixed at Pr = 0.1.

$$\text{Pr} = \frac{\eta_0}{\rho\, \alpha} \tag{2.13}$$

Eckert number (Ec): It is the ratio of the kinetic energy to the enthalpy (or

the dynamic temperature to the temperature) driving force for heat transfer.

$$\mathrm{Ec} = \frac{U^2}{c_p\,\Delta T} \tag{2.14}$$

Buoyancy ratio number (N): It is the ratio between the solute and thermal buoyancy forces and can be either positive or negative, depending on the sign of the concentration volumetric expansion coefficient. For positive values of N, the temperature and concentration buoyancy effects are combined (aiding mode), while for negative values they are opposite (opposing mode). Thus, the buoyancy ratio number has been studied for positive (N = 0.1 and 1) and negative (N = -1) values.

$$\mathrm{N} = \frac{\Delta C\ \beta_T\ D}{\beta_C\ \Delta T\ \alpha} \tag{2.15}$$

Lewis number (Le): It is the ratio of thermal diffusivity to mass diffusivity.

$$\mathrm{Le} = \frac{\alpha}{D} \tag{2.16}$$

Hartmann number (Ha): It is the ratio of electromagnetic force to the viscous force.

$$\mathrm{Ha} = BL\sqrt{\sigma/\eta_0}\ , \tag{2.17}$$

Carreau number (Cu):

$$\mathrm{Cu} = \frac{\lambda\,U}{L} \tag{2.18}$$

Since the buoyancy velocity scale is $U = \left(\frac{\alpha}{L}\right)\mathrm{Ra}^{0.5}$, ΔT and L are equal to unity, the Eckert number has the following relation to the specific heat at constant pressure, Rayleigh number, and thermal diffusivity

$$\mathrm{Ec} \propto \frac{\alpha^2\,\mathrm{Ra}}{c_p}\,, \tag{2.19}$$

The α and c_p for different Carreau fluids in various temperatures can be ranged over (10^{-3} – 10^{-6} m^2/s) and (10^2 – 10^4 J/kg K). So, in the highest studied Rayleigh numbers ($Ra = 10^5$), and the thermal diffusivity ($\alpha = 10^{-3}$) as well as the lowest value of the specific heat at constant pressure, $c_p = 10^2$, the highest amount of the Eckert number would be Ec = 0.001. Therefore, the Eckert number in practical view would be in the range of Ec $\ll$ 0.001. In this study, we have fixed the Eckert number at Ec = 0.001.

The flow domain is given by $\Omega = (0,1) \times (0,1)$, and the boundary $\Gamma = \partial\Omega$. It is the union of six disjoint subsets:

$$\Gamma_1 = \{(x,y), x = 0, 0 \leq y \leq 1\}, \tag{2.20a}$$
$$\Gamma_2 = \{(x,y), x = 1, 0 \leq y \leq 1\}, \tag{2.20b}$$
$$\Gamma_3 = \{(x,y), 0 \leq x \leq 1, y = 0\}, \tag{2.20c}$$
$$\Gamma_4 = \{(x,y), 0 \leq x \leq 1, y = 1\}, \tag{2.20d}$$
$$\Gamma_5 = \left\{(x,y), (x-x_{c1})^2 + (y-y_{c1})^2 = \left(\frac{R_d}{L}\right)^2\right\}, \tag{2.20e}$$
$$\Gamma_6 = \left\{(x,y), (x-x_{c2})^2 + (y-y_{c2})^2 = \left(\frac{R_d}{L}\right)^2\right\}. \tag{2.20f}$$

x_{c1} and y_{c1} are the horizontal and vertical center positions of the first cylinder. x_{c2} and y_{c2} are the horizontal and vertical center positions of the inner second cylinder.

The boundary condition for the velocity is straightforward:

$$\mathbf{u}|_{\Gamma_1} = \mathbf{u}|_{\Gamma_2} = \mathbf{u}|_{\Gamma_3} = \mathbf{u}|_{\Gamma_4} = \mathbf{u}|_{\Gamma_5} = \mathbf{u}|_{\Gamma_6} = \mathbf{0}. \tag{2.21}$$

The boundary conditions for the temperature and concentration are:

$$T|_{\Gamma_1} = T|_{\Gamma_2} = T|_{\Gamma_3} = T|_{\Gamma_4} = T_H, \quad T|_{\Gamma_5} = T|_{\Gamma_6} = T_C \tag{2.22}$$

$$C|_{\Gamma_1} = C|_{\Gamma_2} = C|_{\Gamma_3} = C|_{\Gamma_4} = C_H, \quad C|_{\Gamma_5} = C|_{\Gamma_6} = C_C \tag{2.23}$$

The local and the average Nusselt and Sherwood numbers at the cavity sides are as

$$Nu = \left(-\frac{\partial T}{\partial r}\right)_{r=0}, \quad Sh = \left(-\frac{\partial C}{\partial r}\right)_{r=0}, \tag{2.24a}$$

$$Nu_{avg} = \int_0^1 Nu\, ds, \quad Sh_{avg} = \int_0^1 Sh\, ds \tag{2.24b}$$

where r denotes the unit normal direction on a specific side wall s.

The total average Nusselt and Sherwood numbers are as

$$Nu_{tot_{avg}} = Nu_{L_{avg}} + Nu_{R_{avg}} + Nu_{B_{avg}} + Nu_{T_{avg}} \tag{2.25}$$

$$Sh_{tot_{avg}} = Sh_{L_{avg}} + Sh_{R_{avg}} + Sh_{B_{avg}} + Sh_{T_{avg}} \tag{2.26}$$

In the above equation, the subscribes of tot, L, R, B, T, avg means total, the left wall of the cavity, the right wall of the cavity, the bottom wall of the cavity, the top wall of the cavity, and average; respectively.

3 Entropy generation

The local dimensionless entropy generations with consideration to non-dimensional variables of Eqs. (2.1) - (2.3) can be acquired as follows [2]

$$S_S = S_F + S_T + S_D + S_G \tag{3.1}$$

$$S_F = \Phi_I \left[2\left(\frac{\partial u}{\partial x}\right)^2 + 2\left(\frac{\partial v}{\partial y}\right)^2 + \left(\frac{\partial u}{\partial y} + \frac{\partial v}{\partial x}\right)^2 \right] , \tag{3.2}$$

$$S_T = \left[\left(\frac{\partial T}{\partial x}\right)^2 + \left(\frac{\partial T}{\partial y}\right)^2 \right] , \tag{3.3}$$

$$S_G = \Phi_I \, \mathrm{Ha}^2 \left(u \, sin\theta - v \, cos\theta \right)^2 , \tag{3.4}$$

$$S_D = \Phi_{II} \left[\left(\frac{\partial C}{\partial x}\right)^2 + \left(\frac{\partial C}{\partial y}\right)^2 \right] + \Phi_{III} \left[\left(\frac{\partial C}{\partial x}\right) \left(\frac{\partial T}{\partial x}\right) + \left(\frac{\partial C}{\partial y}\right) \left(\frac{\partial T}{\partial y}\right) \right] , \tag{3.5}$$

$$\Phi_I = \frac{\eta(II(\mathbf{A_1}))\, T_0}{k} \left(\frac{\alpha}{L\Delta T}\right)^2 \mathrm{Ra} , \tag{3.6}$$

$$\delta = \frac{T_0}{k} \left(\frac{\alpha}{L\Delta T}\right)^2 \tag{3.7}$$

$$\Phi_{II} = \frac{RDT_0}{kC_0} \left(\frac{\Delta C}{\Delta T}\right)^2 \tag{3.8}$$

$$\Phi_{III} = \frac{RD}{k} \left(\frac{\Delta C}{\Delta T}\right) \tag{3.9}$$

It should be mentioned that the variables of Φ_{II}, Φ_{III}, δ is taken constant and they are Φ_{II}= 0.5,Φ_{III}= 0.01, δ = 0.0001.

The local non-dimensional Bejan number is calculated as follows:

$$Be = \frac{S_T + S_D}{S_S} , \tag{3.10}$$

The total dimensionless entropy generations are obtained by numerical integration of the local dimensionless entropy generation over the entire cavity volume. It is given by:

$$SF = \int_0^1 \int_0^1 S_F \, dxdy \,, \quad ST = \int_0^1 \int_0^1 S_T \, dxdy, \quad SD = \int_0^1 \int_0^1 S_D \, dxdy, \tag{3.11}$$

$$SG = \int_0^1 \int_0^1 S_G \, dxdy, \; SS = \int_0^1 \int_0^1 S_S \, dxdy, \quad Be_{avg} = \int_0^1 \int_0^1 Be \, dxdy \tag{3.12}$$

4 The numerical method

The FDLBM equations and their relationships with continuum equations have been explained in details in Huilgol and Kefayati [53,54]. Here, just a brief description about the main equations would be cited. In addition, the applied algorithm has been described and the studied problem equations in the FDLBM are mentioned.

4.1 The Continuity and Momentum equations

To have the continuity and momentum equations, a discrete particle distribution function f_α is defined over a D2Q9 lattice where it should satisfy an evolution equation:

$$\frac{\partial f_\alpha}{\partial t} + \boldsymbol{\xi}_\alpha \cdot \nabla_{\mathbf{x}} f_\alpha - F_\alpha = -\frac{1}{\varepsilon \, \phi}(f_\alpha - f_\alpha^{eq}), \tag{4.1}$$

where ε is a small parameter to be prescribed when numerical simulations are considered. ϕ is the relaxation time and F is the external force.

Associated to each node is a lattice velocity vector $\boldsymbol{\xi}_\alpha$. It is defined as follows:

$$\boldsymbol{\xi}_\alpha = \begin{cases} (0,0), & \alpha = 0, \\ \sigma(\cos\Theta_\alpha, \sin\Theta_\alpha) & \alpha = 1,3,5,7, \\ \sigma\sqrt{2}(\cos\Theta_\alpha, \sin\Theta_\alpha), & \alpha = 2,4,6,8. \end{cases} \tag{4.2}$$

Here, the angles Θ_α are defined through $\Theta_\alpha = (\alpha - 1)\pi/4, \; \alpha = 1, \cdots, 8$. The constant σ has to be chosen with care for it affects numerical stability;

its choice depends on the problem. The method for finding the parameter σ which satisfies the Courant-Friedrichs-Lewy (CFL) condition is described in [53,54].

The equilibrium distribution function, f_α^{eq}, is different from the conventional ones adopted by previous researchers, who normally expand the Maxwellian distribution function. In the present approach, we expand f_α^{eq} as a quadratic in terms of $\boldsymbol{\xi}_\alpha$, using the notation of linear algebra [53,54]:

$$f_\alpha^{eq} = A_\alpha + \boldsymbol{\xi}_\alpha \cdot \mathbf{B}_\alpha + (\boldsymbol{\xi}_\alpha \otimes \boldsymbol{\xi}_\alpha) : \mathbf{C}_\alpha, \ \alpha = 0, 1, 2, \cdots, 8. \tag{4.3}$$

Here, the scalars A_α are defined through

$$A_0 = \rho - \frac{2p}{\sigma^2} - \frac{\rho|\mathbf{u}|^2}{\sigma^2} + \frac{\tau_{xx} + \tau_{yy}}{\sigma^2}, \quad A_\alpha = 0, \ \alpha = 1, 2, \cdots, 8. \tag{4.4}$$

The vectors $\mathbf{B}_\alpha$ are given by

$$\mathbf{B}_1 = \frac{\rho \mathbf{u}}{2\sigma^2} = \mathbf{B}_\alpha, \ \alpha = 1, 3, 5, 7; \quad \mathbf{B}_\alpha = \mathbf{0}, \ \alpha = 0, 2, 4, 6, 8. \tag{4.5}$$

Next, the matrices $\mathbf{C}_\alpha$ are such that $\mathbf{C}_0 = 0$; $\mathbf{C}_1 = \mathbf{C}_\alpha$, $\alpha = 1, 3, 5, 7$; $\mathbf{C}_2 = \mathbf{C}_\alpha$, $\alpha = 2, 4, 6, 8$, where

$$\mathbf{C}_1 = \begin{bmatrix} C_{11} & 0 \\ 0 & C_{22} \end{bmatrix}, \quad C_{11} = \frac{1}{2\sigma^4}(p + \rho u^2 - \frac{\mathrm{Pr}}{\sqrt{\mathrm{Ra}}}\tau_{xx}), \quad C_{22} = \frac{1}{2\sigma^4}(p + \rho v^2 - \frac{\mathrm{Pr}}{\sqrt{\mathrm{Ra}}}\tau_{yy}), \tag{4.6}$$

$$\mathbf{C}_2 = \begin{bmatrix} 0 & C_{12} \\ C_{21} & 0 \end{bmatrix}, \quad C_{12} = C_{21} = \frac{1}{8\sigma^4}(\rho uv - \frac{\mathrm{Pr}}{\sqrt{\mathrm{Ra}}}\tau_{xy}). \tag{4.7}$$

The functions F_α in Eq.(4.1) is defined as

$$F_\alpha = 0, \quad \alpha = 0, 2, 4, 6, 8, \tag{4.8a}$$

$$F_\alpha = \frac{1}{2\sigma^2}\mathbf{b} \cdot \boldsymbol{\xi}_\alpha, \quad \alpha = 1, 3, 5, 7 \tag{4.8b}$$

$$\mathbf{b} = \frac{\mathrm{Pr}\,\mathrm{Ha}^2}{\sqrt{\mathrm{Ra}}}\left(v\,sin\theta\,cos\theta - u\,sin^2\theta\right)\mathbf{i} + \left[\mathrm{Pr}\,(T - \mathrm{N}\,C) + \frac{\mathrm{Pr}\,\mathrm{Ha}^2}{\sqrt{\mathrm{Ra}}}\left(u\,sin\theta\,cos\theta - v\,cos^2\theta\right)\right]\mathbf{j} \tag{4.9}$$

4.2 The Energy Equation

In order to obtain the energy equation, an internal energy distribution function g_α is introduced and it is assumed to satisfy an evolution equation similar to that for f_α. Thus,

$$\frac{\partial g_\alpha}{\partial t} + \boldsymbol{\xi}_\alpha \cdot \nabla_{\mathbf{x}} g_\alpha - G_\alpha = -\frac{1}{\varepsilon\phi}(g_\alpha - g_\alpha^{eq}). \tag{4.10}$$

G_α refers to the external supply e.g. radiation in the energy equation. Here, g_α^{eq} has a monomial expansion:

$$g_\alpha^{eq} = D_\alpha + \boldsymbol{\xi}_\alpha \cdot \mathbf{E}_\alpha, \tag{4.11}$$

One way of satisfying the above is to assume, as before, that the scalars are given by $D_\alpha = D_1,\ \alpha = 1, 3, 5, 7$, and $D_\alpha = D_2,\ \alpha = 2, 4, 6, 8,$. In this problem, the non-dimensional parameters are obtained as follows:

$$D_0 = T, \quad D_1 = 0, \quad D_2 = 0. \tag{4.12}$$

where

$$\mathbf{E}_\alpha = 0, \quad \alpha = 0, 2, 4, 6, 8, \tag{4.13a}$$

$$\mathbf{E}_\alpha = \frac{\left(\mathbf{u}\,T - \frac{\mathrm{Pr}\,\mathrm{Ec}}{\sqrt{\mathrm{Ra}}}\ \left((u\,\tau_{xx} + v\,\tau_{xy}) + (u\,\tau_{yx} + v\,\tau_{yy})\right) - \frac{1}{\sqrt{\mathrm{Ra}}}\left(\frac{\partial T}{\partial \mathbf{x}}\right)\right)}{2\,\sigma^2}, \quad \alpha = 1, 3, 5, 7 \tag{4.13b}$$

The parameter G_α can be defined as (See Eqs.3.44–3.48 in Huilgol and Kefayati [53])

$$G_\alpha = 0, \quad \alpha = 0, 2, 4, 6, 8, \tag{4.14a}$$

$$G_\alpha = \frac{\mathrm{Ec}\ \mathrm{Pr}\ \mathrm{Ha}^2}{\sqrt{\mathrm{Ra}}}\left(u\,sin\,\theta - v\,cos\theta\right)^2, \quad \alpha = 1, 3, 5, 7 \tag{4.14b}$$

In order to obtain the concentration equation, an internal concentration distribution function h_α is introduced and it is assumed to satisfy an evolution equation similar to that for f_α. Thus,

$$\frac{\partial h_\alpha}{\partial t} + \boldsymbol{\xi}_\alpha \cdot \nabla_{\mathbf{x}} h_\alpha - H_\alpha = -\frac{1}{\varepsilon\phi}(h_\alpha - h_\alpha^{eq}). \tag{4.15}$$

Here, h_α^{eq} has a monomial expansion:

$$h_\alpha^{eq} = M_\alpha + \boldsymbol{\xi}_\alpha \cdot \mathbf{Z}_\alpha, \tag{4.16}$$

One way of satisfying the above is to assume, as before, that the scalars are given by $M_\alpha = M_1,\ \alpha = 1, 3, 5, 7$, and $M_\alpha = M_2,\ \alpha = 2, 4, 6, 8,$. In this problem, the non-dimensional parameters are obtained as follows:

$$M_0 = C, \quad M_1 = 0, \quad M_2 = 0. \tag{4.17}$$

where

$$\mathbf{Z}_\alpha = 0, \quad \alpha = 0, 2, 4, 6, 8, \tag{4.18a}$$

$$\mathbf{Z}_\alpha = \frac{\left(\mathbf{u}\, C - \frac{1}{\mathrm{Le}\sqrt{\mathrm{Ra}}}\left(\frac{\partial C}{\partial \mathbf{x}}\right)\right)}{2\,\sigma^2}, \quad \alpha = 1, 3, 5, 7 \tag{4.18b}$$

Finally, $H_\alpha = 0$.

5 Code validation and grid independence

Lattice Boltzmann Method (LBM) scheme is utilized to simulate entropy generation of laminar double diffusive natural convection in a heated enclosure that is filled with a Carreau fluid with inner cold cylinders in the presence of a uniform magnetic field. The Prandtl, Lewis, Carreau, and Eckert numbers are fixed at Pr = 0.1, Le = 2.5, Cu = 1, and Ec = 0.001; respectively. This problem is investigated at different parameters of Rayleigh number (Ra = 10^4 and 10^5), Power-law index (n = 0.2, 1, and 1.8), Hartmann number (Ha = 0, 15, 30, 60, and 90), the Buoyancy ratio (N = -1, 0.1, and 1), and the radius of the inner cylinder (R_d = 0.1 L). An extensive mesh testing procedure was conducted to guarantee a grid independent solution. Different mesh combinations were explored for the case of Ra= 10^5, N = 0.1, n = 1.8, and Ha = 15. The average

Nusselt and Sherwood numbers on the hot wall for different meshes and errors have been studied. It was confirmed that the grid size (300*300) ensures a grid independent solution as portrayed by Table.1. The running time for the grid size is 4851 seconds. The applied code for the fluid flow and heat transfer is validated by the study of Park et al. [44] in the Fig.2 at Ra = 10^5, and Pr = 0.71 for the case of cooled enclosure with two heated circular cylinders in the center of the cavity. In addition, the average Nusselt number on the hot circular cylinder, for the case of a cooled enclosure with a single hot circular cylinder, is validated between present results and the studies of Zhang et al. [47], Kim et al. [42], and Park et al. [44] in the Table.2 in different Rayleigh numbers. To demonstrate the accuracy of the present results, MHD natural convection of Newtonian fluids were compared with previous results. In Fig.3, the present code was validated by Pirmohammadi and Ghasemi [13] for MHD natural convection in an enclosure which was filled with liquid gallium (Pr = 0.02) at Ra = 7000 and Ha = 25. In Fig.4, the present code was validated by Sathyamoorthy and Chamkha [14] for MHD natural convection in a liquid gallium filled square cavity for linearly heated side walls (Pr = 0.025) at Ra = 10^5 and Ha = 50. For the validation of the entropy generation study, the local summation entropy generation (S_S) for the case of Ra = 10^5 and Pr = 0.71 has been compared with the study of Mun et al. [50] in Fig.5 which demonstrates a good agreement.

6 Results and discussion

6.1 Effects of Rayleigh number

Fig.6 shows the isotherms, streamlines and isoconcentrations in different Rayleigh numbers at Ha = 15, N = 0.1, and n = 0.2. At Ra = 10^4, the temperature contours are circular around the cylinders which demonstrate the conduction is dominated in the enclosure. As the Rayleigh number increases, the movements of the isotherms between the cold cylinders and hot walls ameliorate significantly and they become progressively curved. Moreover, the gradient of temperature on the hot wall augments with the rise of Rayleigh number. In fact, it occurs while the thermal boundary layer thickness on the side walls decreases with increasing Rayleigh number. The streamlines exhibit that the convection process has been enhanced by the growth of Rayleigh numbers as the core of the streamline changes and the streamlines traverse more distance in the cavity. Secondary circulations can be observed in the validation figure (Fig.2) which compared with the study of Park et al.[44] where the Rayleigh number is equal to Ra = 10^5. It should be noted in the study, the cylinders are hot and the enclosure is cold, so the secondary vortexes are appeared on the top of the cavity and close to the top cylinder. In the studied case here, the

cylinders are cold and the enclosure is hot, so the secondary circulations are appeared in the reverse direction because of the different convection direction and flow movement. The secondary vortexes are disappeared at Ra = 10^4 due to the decrease in convection process and this trend could be confirmed in the Fig.5-h in the the study of Park et al. [44]. The isoconcentration demonstrates a different manner where the increase in Rayleigh number drops the gradient of isoconcentrations on the hot walls. It depicts that mass transfer drops significantly with the rise of Rayleigh number. Table.3 confirms that the average Nusselt and Sherwood numbers enhance as Rayleigh number rises in different power-law indexes for Hartmann numbers of Ha = 0, 15 and 30. In the cited Hartmann numbers also, it is observed that the effect of Rayleigh number drops when the power-law index increases. On the other hand, the increase in Rayleigh number decreases the average Nusselt and Sherwood numbers at Ha = 60 and 90 and this drop is more significant in the average Sherwood number. In addition, it is clear that the effect of power-law index on the average Nusselt and Sherwood numbers declines in the high Hartmann numbers considerably and can be concluded that the rise of Hartmann number diminishes the power-law index influence gradually.

Fig.7 displays the Rayleigh number effects on entropy generations due to heat transfer (S_T), fluid friction (S_F), and mass transfer (S_D) at n = 0.2, Ha = 15, and N = 0.1. It demonstrates that S_T increases generally, but this augmentation is not uniform in the cavity and in some places we face a decrease in the S_T. The S_F demonstrates that the high values are observed on the sidewalls and the surface of the cylinder in both Rayleigh numbers. Generally, the S_F increases considerably with the rise of Rayleigh number where the minimum value in the bottom of the cylinder becomes smaller due to the increase in Rayleigh number. In fact, high values are replaced with the low values at Ra = 10^5 close to the cylinder on the bottom section of the cavity. The entropy generation due to mass transfer (S_D) enhances generally with the rise of Rayleigh number; although, this augmentation is less than S_F. It shows the gradient of S_D on the cylinder enhances with the rise of Rayleigh number. In addition, the entropy generation due to mass transfer in the bottom of the cylinder diminishes as Rayleigh number enhances while close to the bottom wall of the enclosure a high value is generated at Ra = 10^5. Interestingly, the increase in Rayleigh number causes a low value section of S_D is generated on the top section of the enclosure which proves that the rise of Rayleigh number decreases the irreversibility due to mass transfer. Tables.4 and 5 demonstrate that S_T, S_F, and S_D enhance as Rayleigh number increases in various Hartmann numbers and power-law indexes.

Fig.8 illustrates the Rayleigh number effects on entropy generations due to magnetic field (S_G), summation entropy generation (S_S), and the local Bejan number (Be) at n = 0.2, Ha = 15, and N = 0.1. The entropy generation due to magnetic field (S_G) enhances considerably with the rise of Rayleigh

number; although, the shape and distribution of entropy generations (S_G) are nearly the same. The contour of the total entropy generations (S_S) exhibits that the high values are concentrated around the cylinder and sections which are immensely close to the sidewalls for both Rayleigh numbers. Further, it is clear that the main effect on the total entropy generations exhibits are (S_T) and (S_F) at Rayleigh numbers of Ra = 10^4, and Ra = 10^5; respectively. The local Bejan number demonstrates that the Bejan number declines vastly as Rayleigh number increases. However, the top and bottom of the two cylinders are still maximum value at Ra = 10^5. Tables.4 and 5 indicate that different total entropy generations enhance as Rayleigh number increases in various Hartmann numbers and power-law indexes. But, the average Bejan number declines considerably due to the rise of Rayleigh number.

6.2 Effects of power-law index index

Fig.9 shows the isotherms, isoconcentrations and streamlines for different power-law indexes at N = 0.1, Ra = 10^5, Ha = 15. As the power-law index increases, the movements of the isotherms between the cold cylinders and hot walls declines significantly. Moreover, the gradient of temperature on the hot wall augments with the drop of power-law index. In fact, it occurs while the thermal boundary layer thickness on the side walls decreases with the drop of the power-law index. The streamlines exhibit that the convection process has been enhanced by the decrease of power-law index. The isoconcentration shows that the increase in power-law index declines the isoconcentration movement between the hot walls and the cold cylinder. It depicts that mass transfer drops substantially with the rise of power-law index. Table.3 shows that the increase in power-law index in various Hartmann and Rayleigh numbers decreases the average Nusselt and Sherwood numbers. Although, the drop of the average Nusselt and Sherwood numbers decline steadily as Hartmann number rises.

Fig.10 indicates the vertical velocity and temperature in the middle of the cavity, the local Nusselt and sherwood numbers on the left wall have been studied for different power-law indexes at N = 0.1, Ra = 10^5, Ha = 15. Generally, it displays that the vertical velocity for different power-law indexes has the maximum values close to the sidewalls while the minimum magnitudes are observed close to the clod cylinder. The vertical velocity component is essentially negligible in the presence of the cold cylinder. The amplitudes of the vertical velocity magnitude on the top and bottom sides of the cavity do indeed drop with augmentation of power-law index regularly. The local temperature has a curved manner where the minimum values are observed around the cold cylinders and the values decline marginally as power-law index enhances. The local Nusselt and sherwood numbers on the hot wall show sinuously behavior.

They demonstrate that the maximum Nusselt and Sherwood numbers appear at Y = 0.2. Further, the increase in power-law index decreases the local Nusselt and sherwood numbers at $Y < 0.5$ while they do not change significantly due to the rise of the power-law index at $Y > 0.5$.

Fig.11 depicts the power-law index effects on entropy generations due to heat transfer (S_T), fluid friction (S_F), mass transfer (S_D), and magnetic field (S_G) at N = 0.1, Ra = 10^5, Ha = 15. It shows that the S_T becomes weak slightly as the power-law index increases. The bottom side of the enclosure can demonstrate the effect of power-law index on the S_T clearly where the high values of S_T = 60 and 40 at n=0.2 disappears at n=1.8. However, the increase in power-law index does not influence the top section of cylinder in S_T. The enhancement of power-law index from n = 0.2 to 1.8 enhances the values in the contours of S_F marginally where the S_F = 10 can distinguish this pattern. But, the values of S_F declines from n = 1 to 1.8. It also displays that the values in the contours of S_D weakens steadily as the power-law index enhances. The bottom wall of the enclosure demonstrates that the S_D = 20 diminishes with the rise of power-law index. It should also be noted that the low value on the top of the enclosure is not affected by the change of the power-law index. The contour of the local entropy generation due to magnetic field demonstrates S_G weakens gradually as power-law index rises. Tables.4 and 5 state that rise of power-law index decreases the S_T, S_F, S_D, and S_G for different Rayleigh numbers. However, it depicts that the effect of power-law index on the studied entropy generations decline vastly as Hartmann number drops.

Fig.12 displays the power-law index effects on entropy generations due to summation entropy generation (S_S), and the local Bejan number (Be) at N = 0.1, Ra = 10^5, Ha = 15. The contours of the total entropy generation show that the values of S_S declines slightly as the power-law index enhances. It depicts that the local Bejan number alters slightly with the rise of power-law index. Tables.4 and 5 indicate that the change of power-law index alters the total entropy generation and the average Bejan number irregularly in different Rayleigh and Hartmann numbers. However, it is obvious the SS and Be_{avg} are not affected by the rise of power-law indexes in High values of Hartmann numbers (Ha = 30, 60, and 90).

6.3 Effects of Hartmann number

Fig.13 exhibits the isotherms, isoconcentrations and streamlines for different Hartmann numbers at n = 0.2, N = 0.1, Ra = 10^5. it is apparent that the presence of the magnetic field results in the drop of the convection process in the isotherms as the curved shape of the isotherms alter to linear ones and also their movements between cylinders and walls decrease immensely. The same

pattern is observed in isoconcentrations where the convection of mass transfer between the cold cylinders and hot walls drop steadily as Hartmann number rises. The streamlines confirm the decrease in convection evidently since two curved main circulations alter and two small vortexes on the bottom of the cavity disappears. Table.3 shows that the increase in Hartmann number causes the average Nusselt and Sherwood numbers to drop considerably in various Rayleigh numbers and power-law indexes.

Fig.14 indicates the vertical velocity and temperature in the middle of the cavity, the local Nusselt and sherwood numbers on the left wall have been studied for different power-law indexes at n = 0.2, N = 0.1, Ra = 10^5. Generally, it displays that the vertical velocity for different Hartmann numbers has the maximum values close to the sidewalls while the minimum magnitudes are observed close to the clod cylinder. The vertical velocity component is essentially negligible in the presence of the cold cylinder. The amplitudes of the vertical velocity magnitude on the top and bottom sides of the cavity do indeed drop with augmentation of Hartmann number regularly. The local Nusselt and sherwood numbers on the hot wall show sinuously behavior. They demonstrate that the maximum Nusselt and Sherwood numbers appear at Y = 0.2. Further, the increase in Hartmann number decreases the local Nusselt and sherwood numbers at $Y < 0.5$ while they enhance marginally due to the rise of the Hartmann number at $Y > 0.5$.

Fig.15 displays the Hartmann number effect on entropy generations due to heat transfer (S_T), fluid friction (S_F), mass transfer (S_D), and magnetic field (S_G) at Ra = 10^5, n = 0.2, N = 0.1. It shows that the S_T becomes weak slightly as the Hartmann number increases. The bottom side of the enclosure can demonstrate the effect of Hartmann number on the S_T clearly where the high values of S_T = 60 and 40 at Ha = 0 disappears at Ha = 90. However, the increase in Hartmann number does influence the top section of cylinder in S_T marginally. The enhancement of Hartmann number from Ha = 0 to 90 diminishes the values in the contours of S_F significantly where the $S_F = 1$ can distinguish this pattern. It also displays that the values in the contours of S_D weakens steadily as the Hartmann number enhances. The bottom wall of the enclosure demonstrates that the S_D = 60 diminishes with the rise of Hartmann number. It should also be noted that the low value on the top of the enclosure is not affected by the change of the Hartmann number. The contour of the local entropy generation due to magnetic field demonstrates S_G decreases gradually as Hartmann number rises. Tables.4 and 5 display that different entropy generations of S_T, S_F, S_D, and S_G decrease gradually as Hartmann number increases.

Fig.16 illustrates the Hartmann number effect on entropy generations due to summation entropy generation (S_S), and the local Bejan number (Be) at Ra = 10^5, n = 0.2, N = 0.1. The contours of the total entropy generation show

that the values of S_S declines considerably as the Hartmann number enhances. It depicts that the maximum values sections of local Bejan number expand as Hartmann number rises. Tables.4 and 5 demonstrate that S_S and Be_{avg} alter as Hartmann number increases. It is observed that the average Bejan number changes slightly since Hartmann number increases.

6.4 Effects of Buoyancy ratio

Fig.17 depicts the isotherms, streamlines and the isoconcentrations for different buoyancy ratios at Ra = 10^5, n = 1.8, Ha = 15. The comparison between the isotherms demonstrates the rise of the buoyancy ratio from N = -1 to 1 causes the gradient of the isotherms increase significantly. Hence, the pattern clarifies that the augmentation of buoyancy ratio enhances heat transfer. Moreover, the trend is observed in isoconcentrations as they incline to the hot wall and their gradient augments noticeably. As a result, mass transfer similar to heat transfer is improved by the increase in buoyancy ratio. The shapes of the streamlines in different buoyancy ratios can prove the cited result in the isotherms and isoconcentrations properly. At N = -1, vortexes close to the cold cylinders are observed at N=-1. It is evident that the circulations close to the cold cylinders disappear as buoyancy ratio enhances from N = -1 to 0.1. The main circulation becomes stronger when the buoyancy ratio increases from N = 0.1 to 1. Table.6 cites that the increase in Buoyancy ratio from N=-1 to 1 enhance the average Nusselt and Sherwood numbers gradually.

Fig.18 shows the Buoyancy ratio effects on entropy generations due to heat transfer (S_T), fluid friction (S_F), mass transfer (S_D), summation entropy generation (S_S), and the local Bejan number (Be) at n = 1.8, Ra = 10^5, Ha = 15. It demonstrates that the local entropy generation due to heat transfer changes considerably as the buoyancy ratio increases from N = -1 to 0.1 where the values augment considerably and the values of S_T and their gradients around cylinders augments and two sections of high values are observed on the bottom side of the cavity. The augmentation of S_T continues from N = 0.1 to 1, but the shape is the same as N=0.1. The local entropy generation due to fluid friction has changed utterly as the buoyancy ratio increases from N = -1 to 0.1 where the maximum values are formed close to the cylinder at N = 1. The S_F augments considerably in the contours at N= 1. The local entropy generation due to mass transfer strengthens as the buoyancy ratio increases where the values of S_D in bottom side of the cavity can distinguish the enhancement clearly. The local entropy generation due to magnetic field enhances as the buoyancy ratio rises; although, the pattern is the same for different buoyancy ratios. The local contours of the summation entropy generation S_S demonstrates that the increase in buoyancy ratio augments the values around the cylinder although small sections with low values bottom of

the cylinder are generated. The local Bejan number displays that the rise of buoyancy ratio from N = -1 to 0.1 diminishes the high values in the middle of the cavity considerably. The decrease in the local Bejan number continues at N=1; although, this reduction is not extensive. Table.7 indicates that different entropy generations rise since the Buoyancy ratio increases from N = -1 to 1. But, the average Bejan number declines steadily from N = -1 to 1.

7 Concluding Remarks

Thermosolutal natural convection and entropy generation of Carreau fluid in the presence of a uniform magnetic field in a cavity in the presence of two cylinders has been analysed by Lattice Boltzmann method. This study has been conducted for the pertinent parameters in the following ranges: Rayleigh number (Ra = 10^4 and 10^5), the Buoyancy ratio (N = -1, 0.1, 1), Hartmann numbers (Ha = 0, 15, 30, 60 and 90), and power-law indexes (n = 0.2, 1, and 1.8). The main conclusions of the present investigation can be summarized as follows:

- Heat and mass transfer enhance as Rayleigh number augments in different studied parameters. However, the alterations of Hartmann number and power-law index affect the enhancement significantly.
- The average Nusselt and Sherwood numbers demonstrate that the heat and mass transfer decline since the power-law index rises in various studied parameters. Although, the increase in Rayleigh number and the decline of Hartmann number strengthen the effect of power-law index.
- The enhancement of the buoyancy ratio increases heat and mass transfer considerably at Ra = 10^5, but the rise of buoyancy ratio has marginal effect on the increase in heat and mass transfer at Ra = 10^4.
- The heat and mass transfer decreases substantially as Hartmann number increases from Ha = 0 to 30 for different studied parameters. But, at Ha = 60 and 90, the effect of the magnetic field on heat and mass transfer is marginal.
- It was observed that the effect of power-law index on heat and mass transfer drops as Hartmann number rises.
- The enhancement of Rayleigh number augments different irreversibilities and the highest level of growth is observed at the entropy generation due to fluid friction.
- Bejan number declines significantly with the augmentation of Rayleigh number which demonstrates a jump in the irreversibility due to fluid friction.
- The enhancement of power-law index decreases different entropy generations steadily while the average Bejan number changes marginally.
- The increase in the buoyancy ratio enhances the entropy generations and causes the average Bejan number to drop.

- The rise of Hartmann number decreases the total entropy generation and provokes the average Bejan number to alter slightly.

Acknowledgements

The first author(Gholamreza Kefayati (GH. R. Kefayati)) gratefully acknowledges the funding support in the form of a Research Fellowship awarded him by the Hong Kong Polytechnic University.

References

[1] GH.R. Kefayati, H. Tang, Double-diffusive natural convection and entropy generation of Carreau fluid in a heated enclosure with an inner circular cold cylinder (Part I: Heat and mass transfer), International Journal of Heat and Mass Transfer 120 (2018) 731–750.

[2] GH.R. Kefayati, H. Tang, Double-diffusive natural convection and entropy generation of Carreau fluid in a heated enclosure with an inner circular cold cylinder (Part II: Entropy generation), International Journal of Heat and Mass Transfer 120 (2018) 683–713.

[3] R. Bennacer, D. Gobin, Cooperating thermosolutal convection in enclosures I. Scale analysis and mass transfer, lnt. J. Heat Mass Transfer. Vol. 39 (1996) 2671–2681.

[4] R. Bennacer, D. Gobin, Cooperating thermosolutal convection in enclosures II. Heat transfer and flow structure, lnt. J. Heat Mass Transfer, 39 (1996) 2683–2697.

[5] S.H. Xin, P.L. Qur, L.S. Tuckerman, Bifurcation analysis of double-diffusive convection with opposing horizontal thermal and solutal gradients, Phys. Fluids 10 (1998) 850–858.

[6] I. Sezai, Three-dimensional double-diffusive convection in a porous cubic enclosure due to opposing gradients of temperature and concentration, J. Fluid Mech. 400 (1999) 333–353.

[7] I. Sezai, A. A. Mohamad, Double diffusive convection in a cubic enclosure with opposing temperature and concentration gradients, Phys. Fluids 12 (2000) 2210–2223.

[8] I. Sezai, Flow transitions in three-dimensional double-diffusive fingering convection in a porous cavity, J. Fluid Mech. 464 (2002) 311–344.

[9] GH.R. Kefayati, FDLBM simulation of entropy generation in double diffusive natural convection of power-law fluids in an enclosure with Soret and Dufour effects, Int. J. Heat Mass Transfer 89 (2015) 267–290.

[10] Q.Y. Zhu, Y.J. Zhuang, H.Z. Yu, Three-dimensional numerical investigation on thermosolutal convection of power-law fluids in anisotropic porous media, International Journal of Heat and Mass Transfer 104 (2017) 897–917.

[11] Q.Y. Zhu, Y.J. Zhuang, H.Z. Yu, Entropy generation due to three-dimensional double-diffusive convection of power-law fluids in heterogeneous porous media, International Journal of Heat and Mass Transfer 106 (2017) 61–82.

[12] M. Sheikholeslami, H. B. Rokni, Simulation of nanofluid heat transfer in presence of magnetic field: A review. Int. J. Heat & Mass Transfer, 115 (2017) 1203–1233.

[13] M. Pirmohammadi, M. Ghassemi, Effect of magnetic field on convection heat transfer inside a tilted square enclosure, Int. Comm. Heat and Mass Transfer, 36 (2009) 776–780.

[14] M. Sathiyamoorthy, A. Chamkha, Effect of magnetic field on natural convection flow in a liquid gallium filled square cavity for linearly heated side wall(s), Int. J. Therm. Sci., 49 (2010) 1856–1865.

[15] S. Sivasankaran, A. Malleswaran, J. Lee, P. Sundar, Hydro-magnetic combined convection in a lid-driven cavity with sinusoidal boundary conditions on both sidewalls, Int. J. Heat Mass Transfer, 54 (2011) 512–525.

[16] M. M. Rahman, S. Parvin, R. Saidur, N. A. Rahim, Magnetohydrodynamic mixed convection in a horizontal channel with an open cavity, Int. Commun. Heat Mass Transfer, 38 (2011) 184–193.

[17] H. F. Oztop, K. Al-Salem, I. Pop, MHD mixed convection in a lid-driven cavity with corner heater, Int. J. Heat Mass Transfer, 54 (2011) 3494–3504.

[18] R. Nasrin, S. Parvin, Hydromagnetic effect on mixed convection in a lid-driven cavity with sinusoidal corrugated bottom surface, Int. Commun. Heat Mass Transfer, 38 (2011) 781–789.

[19] R. Yousofvand, S. Derakhshan, K. Ghasemi, M. Siavashi, MHD transverse mixed convection and entropy generation study of electromagnetic pump including a nanofluid using 3D LBM simulation, International Journal of Mechanical Sciences 133 (2017) 73–90.

[20] S. A. M. Mehryan, Mohammad Ghalambaz, Muneer A. Ismael, Ali J. Chamkha, Analysis of fluid-solid interaction in MHD natural convection in a square cavity equally partitioned by a vertical flexible membrane, Journal of Magnetism and Magnetic Materials 424 (2017) 161–173.

[21] Mohammad Ghalambaz, Ali Doostanidezfuli, Hossein Zargartalebi, Ali J. Chamkha, MHD phase change heat transfer in an inclined enclosure: Effect of a magnetic field and cavity inclination, Numerical Heat Transfer, Part A: Applications 71 (2017) 91–109.

[22] Fatih Selimefendigil, Hakan F.Oztop, Numerical study of MHD mixed convection in a nanofluid filled lid driven square enclosure with a rotating cylinder, International Journal of Heat and Mass Transfer 78 (2014) 741–754.

[23] Fatih Selimefendigil, Hakan F. Oztop, Conjugate natural convection in a nanofluid filled partitioned horizontal annulus formed by two isothermal cylinder surfaces under magnetic field, International Journal of Heat and Mass Transfer 108 (2017) 156–171.

[24] Nadezhda S. Bondareva, Mikhail A. Sheremet, Natural convection heat transfer combined with melting process in a cubical cavity under the effects of uniform inclined magnetic field and local heat source, International Journal of Heat and Mass Transfer 108 (2017) 156–171.

[25] Nikita S. Gibanov, Mikhail A. Sheremet, Hakan F. Oztop, Nidal Abu-Hamdeh, Effect of uniform inclined magnetic field on mixed convection in a lid-driven cavity having a horizontal porous layer saturated with a ferrofluid, International Journal of Heat and Mass Transfer 114 (2017) 1086–1097.

[26] Jong Hyeon Son , Il Seouk Park, Numerical study of MHD natural convection in a rectangular enclosure with an insulated block, Numerical Heat Transfer, Part A 71 (2017) 1004–1022.

[27] A.J. Chamkha, Hydromagnetic Combined Convection Flow in a Vertical Lid-Driven Cavity Enclosure with Internal Heat Generation or Absorption, Numerical Heat Transfer, Part A, 41 (2002) 529–546.

[28] M. Sheikholeslami, A.J. Chamkha, Flow and Convective Heat Transfer of a Ferro-Nanofluid in a Double-Sided Lid-Driven Cavity with a Wavy Wall in the Presence of a Variable Magnetic Field, Numerical Heat Transfer, Part A, 69 (2016) 1186–1200.

[29] F. Selimefendigil, H. Oztop, A.J. Chamkha, FluidStructure-Magnetic Field Interaction in a Nanofluid Filled Lid-Driven Cavity with Flexible Side Wall, European Journal of Mechanics B/Fluids, 61 (2017) 77–85.

[30] F. Selimefendigil, A.J. Chamkha, MHD Mixed Convection in a Lid-Driven Cavity Having a Corrugated Bottom Wall and Filled with a Non-Newtonian Power-Law Fluid Under the Influence of an Inclined Magnetic Field, ASME Journal of Thermal Science and Engineering Applications, 8 (2016) 021023-1—021023-8.

[31] M. Sheikholeslami, S. A. Shehzad, Numerical analysis of Fe3O4H2O nanofluid flow in permeable media under the effect of external magnetic source, International Journal of Heat and Mass Transfer 118 (2018) 182–192.

[32] M. Sheikholeslami, S. A. Shehzad, Magnetohydrodynamic nanofluid convection in a porous enclosure considering heat flux boundary condition, International Journal of Heat and Mass Transfer 106 (2017) 1261–1269.

[33] M. Sheikholeslami, S. A. Shehzad, Thermal radiation of ferrofluid in existence of Lorentz forces considering variable viscosity, International Journal of Heat and Mass Transfer 109 (2017) 82–92.

[34] M. Sheikholeslami, S. A. Shehzad, Magnetohydrodynamic nanofluid convective flow in a porous enclosure by means of LBM, International Journal of Heat and Mass Transfer 113 (2017) 796–805.

[35] M. Sheikholeslami, S. A. Shehzad, CVFEM for influence of external magnetic source on Fe3O4-H2O nanofluid behavior in a permeable cavity considering shape effect, International Journal of Heat and Mass Transfer 115 (2017) 180–191.

[36] F. Czerwinski, Magnesium Injection Molding, Springer, New York, 2008.

[37] P. J. Carreau, Rheological equations from molecular network theories, Trans Soc Rheol 16 (1972) 99-127.

[38] A. Shamekhi, K. Sadeghy, Cavity flow simulation of CarreauYasuda non-Newtonian fluids using PIM meshfree method, Applied Mathematical Modelling 33 (2009) 4131-4145.

[39] M. Bouteraa, C. Nouar1, E. Plaut, C. Metivier, A. Kalck, Weakly nonlinear analysis of Rayleigh Benard convection in shear-thinning fluids: nature of the bifurcation and pattern selection, J. Fluid Mech. 767 (2015) 696-734.

[40] A. Pantokratoras, Steady flow of a non-Newtonian Carreau fluid across an unconfined circular cylinder, Meccanica 51 (2016) 1007-1016.

[41] S. Shahsavari, G. H. McKinley, Mobility of Power-law and Carreau Fluids through Fibrous Media, Physical review E, Statistical, nonlinear, and soft matter physics 92 (2015) pp.063012.

[42] B.S. Kim, D.S. Lee, M.Y. Ha, H.S. Yoon, A numerical study of natural convection in a square enclosure with a circular cylinder at different vertical locations, International Journal of Heat and Mass Transfer 51 (2008) 1888–1906.

[43] A. A. Mehrizi, K. Sedighi, M. Farhadi, M. Sheikholeslami, Lattice Boltzmann simulation of natural convection heat transfer in an elliptical-triangular annulus, International Communications in Heat and Mass Transfer 48 (2013) 164–177.

[44] Yong Gap Park, Man Yeong Ha, Changyoung Choi, Jaehyun Park, Natural convection in a square enclosure with two inner circular cylinders positioned at different vertical locations, International Journal of Heat and Mass Transfer 77 (2014) 501-518.

[45] A. A. Mehrizi, A. A. Mohamad, Effect of the Inclination Angle and Eccentricity on Free Convection Heat Transfer in EllipticalTriangular Annuli: A Lattice Boltzmann Approach, Numerical Heat Transfer, Part A: Applications 68 (2015) 17–43.

[46] Young Min Seo, Yong Gap Park, Minsung Kim, Hyun Sik Yoon, Man Yeong Ha, Two-dimensional flow instability induced by natural convection in a square enclosure with four inner cylinders. Part I: Effect of horizontal position of inner cylinders, International Journal of Heat and Mass Transfer 113 (2017) 1306–1318.

[47] Ping Zhang, Xiaohua Zhang, Jiheng Deng, Laizhong Song, A numerical study of natural convection in an inclined square enclosure with an elliptic cylinder using variational multiscale element free Galerkin method, International Journal of Heat and Mass Transfer 99 (2016) 721–737.

[48] G.G. Ilis, M. Mobedi, B. Sunden, Effect of aspect ratio on entropy generation in a rectangular cavity with differentially heated vertical walls, International Communications in Heat and Mass Transfer 35 (2008) 696-703.

[49] W. M. El-Maghlany, K.M. Saqr, M. A. Teamah, Numerical simulations of the effect of an isotropic heat field on the entropy generation due to natural convection in a square cavity, Energy Conversion and Management 85 (2014) 333-342.

[50] Gi Su Mun, Jeong Hoon Doo, Man Yeong Ha, Thermo-dynamic irreversibility induced by natural convection in square enclosure with inner cylinder. Part-I: Effect of tilted angle of enclosure, International Journal of Heat and Mass Transfer 97 (2016) 1102-1119.

[51] Jeong Hoon Doo, Gi Su Mun, Man Yeong Ha, Seon Yoo Seong, Thermo-dynamic irreversibility induced by natural convection in square enclosure with inner cylinder. Part-II: Effect of vertical position of inner cylinder, International Journal of Heat and Mass Transfer 97 (2016) 1120-1139.

[52] S.C. Fu, R.M.C. So, W.W.F. Leung, Linearized-Boltzmann-type-equation-based finite difference method for thermal incompressible flow, Computers and Fluids 69 (2012) 67-80.

[53] R. R. Huilgol, GH. R. Kefayati, From mesoscopic models to continuum mechanics: Newtonian and non-Newtonian fluids, Journal of Non-Newtonian Fluid Mechanics 233 (2016) 146-154.

[54] R. R. Huilgol, GH. R. Kefayati, A particle distribution function approach to the equations of continuum mechanics in Cartesian, cylindrical and spherical coordinates: Newtonian and non-Newtonian Fluids, Journal of Non-Newtonian Fluid Mechanics 251 (2018) 119–131.

Nomenclature

$\mathbf{A_1}$ The first Rivlin–Ericksen tensor
B The magnetic field
Be Bejan number
$\mathbf{b}$ Body force
C Concentration
c Lattice speed
c_p Specific heat capacity at constant pressure
Cu Carreau number
D Mass diffusivity
Ec Eckert number
F External forces
f_α Density distribution functions for the specific node of α
f_α^{eq} Equilibrium density distribution functions for the specific node of α
g_α Internal energy distribution functions for the specific node of α
g_α^{eq} Equilibrium internal energy distribution functions for the specific node of α
g Gravity
h_α Internal concentration distribution functions for the specific node of α
h_α^{eq} Equilibrium internal concentration distribution functions for the specific node of α
Ha Hartmann number
k Thermal conductivity
L Length of the cavity
Le Lewis number
n Power-law index
N Buoyancy ratio
Nu Nusselt number
p Pressure
Pr Prandtl number
R Gas constant
Ra Rayleigh number
R_d Radius of the inner circular cylinder
Sh Sherwood number
S_D Local entropy generation due to mass transfer
S_F Local entropy generation due to fluid friction
S_G Local entropy generation due to magnetic field
S_T Local entropy generation due to heat transfer
SD Total entropy generation due to mass transfer
SF Total entropy generation due to fluid friction
SG Total entropy generation due to magnetic field
ST Total entropy generation due to heat transfer
T Temperature

t Time
x, y Cartesian coordinates
x_c, y_c The horizental and vertical positions of the cylinder center
u Velocity in x direction
v Velocity in y direction

Greek letters

β_T Thermal expansion coefficient
β_C Solutal expansion coefficient
ϕ Relaxation time
τ Shear stress
ξ Discrete particle speeds
Δx Lattice spacing
Δt Time increment
α Thermal diffusivity
ρ Density of fluid
η Dynamic viscosity
η_0 Zero shear viscosity
η_∞ Infinite shear viscosity
ψ Stream function value
λ Time constant
σ Electrical conductivity

Subscripts

avg Average
B Bottom
C Cold
c Center
d Dynamic
H Hot
L Left
x, y Cartesian coordinates
α Specific node
R Right
T Thermal, Top
tot Total
D Solutal

Table 1
Grid independence study at Ra = 10^5, n = 1.8, Ha = 15, and N = 0.1

Mesh size	Nu_{avg}	Error	Sh_{avg}	Error
150*150	7.3252	8.07%	6.3325	8.18%
200*200	7.0852	4.53%	6.1863	5.69%
250*250	6.8802	1.50%	5.9462	1.59%
300*300	6.7779	0%	5.8533	0%
350*350	6.7779	0%	5.8533	0%

Table 2
Comparison of the average Nusselt number on the hot circular cylinder between the present result and previous studies for Newtonian fluids in different Rayleigh numbers for the case of the concentric hot cylinders in the cold cavity

	Present study	Zhang et al. [47]	Kim et al. [42]	Park et al. [44]
Ra = 10^3	5.105	5.103	5.093	5.107
Ra = 10^4	5.116	5.087	5.108	5.128
Ra = 10^5	7.791	7.651	7.767	7.836

Table 3
The average Nusselt and Sherwood numbers in various Rayleigh numbers, power-law indexes, and Hartmann numbers at N = 0.1

		Ha = 0	Ha = 15	Ha = 30	Ha = 60	Ha = 90
Ra = 10^4						
Nu_{avg}	n=0.2	7.0221	6.7147	6.5893	6.5651	6.5631
	n=1	6.8060	6.6682	6.5865	6.5652	6.5631
	n=1.8	6.7276	6.6470	6.5847	6.5652	6.5631
Sh_{avg}	n=0.2	7.6163	6.5132	5.9274	5.7910	5.7776
	n=1	6.8428	6.3036	5.9111	5.7906	5.7776
	n=1.8	6.5431	6.2054	5.9009	5.7904	5.7776
Ra = 10^5						
Nu_{avg}	n=0.2	9.2741	8.2650	6.6718	5.5129	5.3263
	n=1	7.8980	7.3164	6.3387	5.4913	5.3243
	n=1.8	7.1187	6.7779	6.1402	5.4758	5.3227
Sh_{avg}	n=0.2	11.2962	9.3586	6.1600	3.4728	2.9017
	n=1	8.0728	7.0569	5.2647	3.3950	2.8931
	n=1.8	6.4070	5.8533	4.7566	3.3375	2.8856

Table 4
Different entropy generations and average Bejan numbers in various Hartmann numbers and power-law indexes at Ra = 10^4 and N = 0.1

	ST	SF	SD	SG	SS	Be_{avg}
Ha = 0						
n=0.2	6.9858	0.8841	4.2753	0	12.14543	0.8344
n=1	6.7759	0.8052	3.9008	0	11.4820	0.8407
n=1.8	6.6942	0.7158	3.7417	0	11.1517	0.8476
Ha = 15						
n=0.2	6.6782	0.3828	3.7152	0.3105	11.0869	0.8441
n=1	6.6327	0.3635	3.6140	0.2544	10.8648	0.8523
n=1.8	6.6112	0.3503	3.5639	0.2272	10.7527	0.8575
Ha = 30						
n=0.2	6.5534	0.1043	3.4224	0.2394	10.3196	0.8871
n=1	6.5505	0.1046	3.4146	0.2253	10.2951	0.8893
n=1.8	6.5488	0.1056	3.4096	0.2175	10.2816	0.8906
Ha = 60						
n=0.2	6.5297	0.0191	3.3558	0.1037	10.0083	0.9221
n=1	6.5296	0.0193	3.3557	0.1028	10.0073	0.9223
n=1.8	6.5295	0.0195	3.3556	0.1021	10.0066	0.9224
Ha = 90						
n=0.2	6.5274	0.0064	3.3494	0.0556	9.9388	0.9335
n=1	6.5274	0.0064	3.3494	0.0554	9.9387	0.9336
n=1.8	6.5275	0.0064	3.3494	0.0553	9.9386	0.9336

Table 5
Different entropy generations and average Bejan numbers in various Hartmann numbers and power-law indexes at Ra = 10^5 and N = 0.1

	ST	SF	SD	SG	SS	Be_{avg}
Ha = 0						
n=0.2	10.0988	14.8228	7.8767	0	32.7985	0.4154
n=1	9.1831	19.5019	6.8366	0	35.5217	0.3850
n=1.8	8.5171	21.1596	6.0767	0	35.7536	0.3728
Ha = 15						
n=0.2	9.3198	11.1837	7.1442	7.5452	35.1929	0.3577
n=1	8.6349	14.2812	6.3156	7.6838	36.9157	0.3380
n=1.8	8.1610	15.5631	5.7487	7.7093	37.1823	0.3294
Ha = 30						
n=0.2	7.9186	5.8592	5.6765	14.1260	33.5805	0.3659
n=1	7.6640	6.8727	5.3240	13.8140	33.6749	0.3569
n=1.8	7.4909	7.4973	5.0852	13.6046	33.6782	0.3516
Ha = 60						
n=0.2	6.8687	1.4658	4.3591	9.0010	21.6947	0.4669
n=1	6.8527	1.5791	4.3314	8.8261	21.5892	0.4657
n=1.8	6.8404	1.6991	4.3095	8.7479	21.5971	0.4646
Ha = 90						
n=0.2	6.7056	0.5210	4.1021	5.1181	16.4467	0.5577
n=1	6.7040	0.5444	4.0993	5.0777	16.4254	0.5575
n=1.8	6.7027	0.5720	4.0969	5.0575	16.4290	0.5573

Table 6
Effects of the Buoyancy ratio (N) on the average Nusselt and Sherwood numbers in different Rayleigh numbers at n = 1.8, Ha = 15

	N=0.1	N=1	N=-1
Ra = 10^4			
Nu_{avg}	6.6470	6.7682	6.5631
Sh_{avg}	6.2054	6.7803	5.7772
Ra = 10^5			
Nu_{avg}	6.7779	7.8719	5.3899
Sh_{avg}	5.8533	8.0754	2.8022

Table 7
Effects of the Buoyancy ratio (N) on different entropy generations and average Bejan number in different Rayleigh numbers at n = 1.8, Ha = 15

	N=0.1	N=1	N=-1
Ra = 10^4			
ST	6.6112	6.7326	6.5270
SF	0.3503	1.0042	0.0018
SD	3.5639	3.8467	3.3482
SG	0.2272	0.6048	0.0009
SS	10.7527	12.1884	9.8779
Be_{avg}	0.8575	0.7644	0.9471
Ra = 10^5			
ST	81610	9.2036	6.8213
SF	15.5631	32.4964	0.9438
SD	5.7487	6.8825	4.1509
SG	7.7093	13.5848	0.5787
SS	37.1823	62.1674	12.4948
Be_{avg}	0.3294	0.2651	0.6881

List of Figures

Fig.11 Contours of the local entropy generations due to heat transfer (S_T), fluid friction (S_F), mass transfer (S_D), magnetic field (S_G) for different power-law indexes at Ra = 10^5, Ha = 15, N = 0.1

Fig.12 Contours of the local entropy due to the summation entropy generation (S_S), and the local Bejan number (Be) for different power-law indexes at Ra = 10^5, Ha = 15, N = 0.1

Fig.13 Comparison of the isotherms, streamlines, and isoconcentrations for different Hartmann numbers at n=0.2, N = 0.1, Ra = 10^5

Fig.14 Comparisons of local Nusselt and Sherwood numbers on the left hot wall, velocity and temperature distributions in the middle of the cavity for different Hartmann numbers at n = 0.2, N = 0.1, Ra = 10^5

Fig.15 Contours of the local entropy generations due to heat transfer (S_T), fluid friction (S_F), magnetic field (S_G), and mass transfer (S_D) for different Hartmann numbers at Ra = 10^5, n = 0.2, N = 0.1

Fig.16 Contours of the local entropy due to the summation entropy generation (S_S), and the local Bejan number (Be) for different Hartmann numbers at Ra = 10^5, n = 0.2, N = 0.1

Fig.17 Comparison of the isotherms, streamlines, and isoconcentrations for different Buoyancy ratios at Ra = 10^5, n = 1.8, Ha = 15

Fig.18 Effects of the Buoyancy ratio (N) on the local entropy generations due to heat transfer (S_T), fluid friction (S_F), mass transfer (S_D), summation entropy generation (S_S), and the local Bejan number (Be) at n = 1.8, Ra = 10^5, Ha = 15

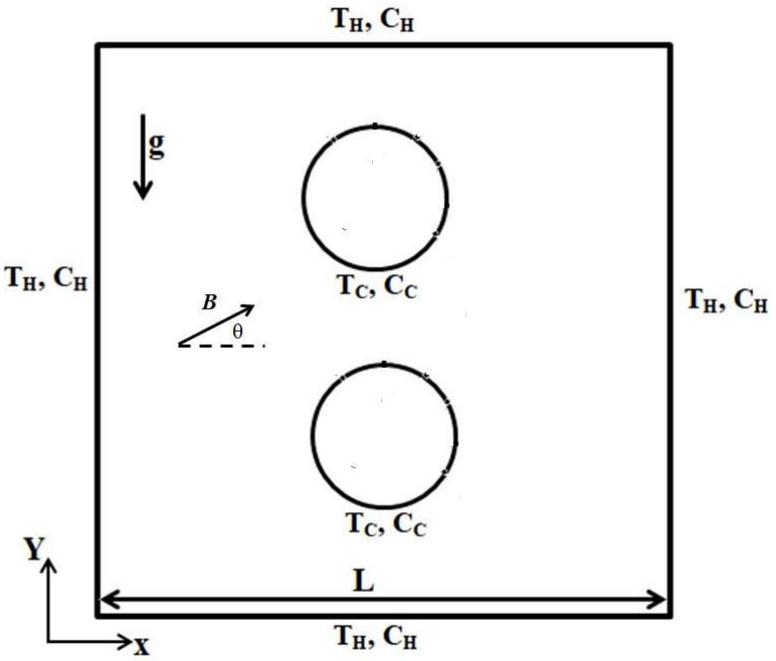

Fig. 1. Geometry of present study

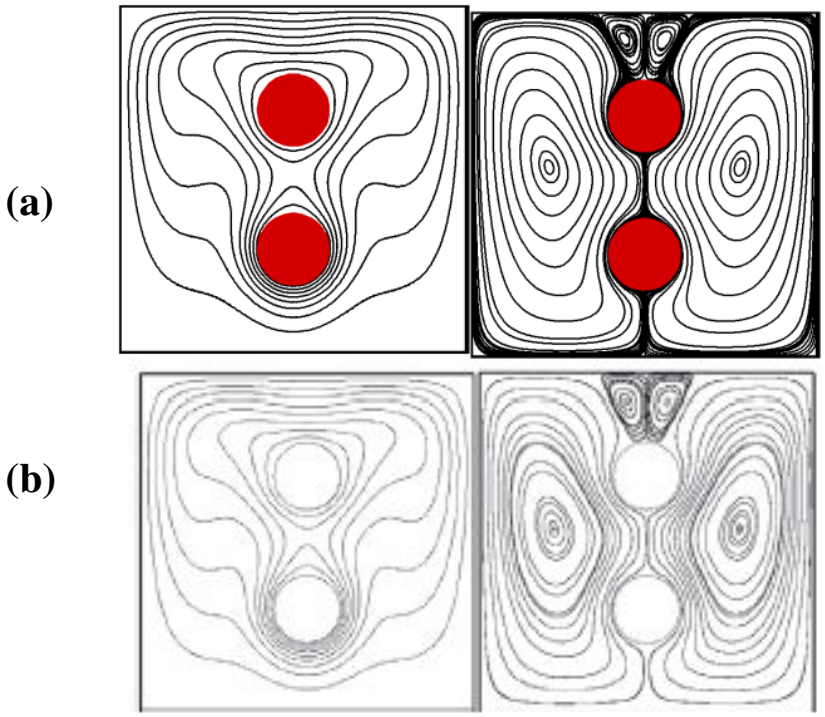

Fig. 2. The comparison of the isotherms and streamlines between (a) present study and (b) Park et al. [44]

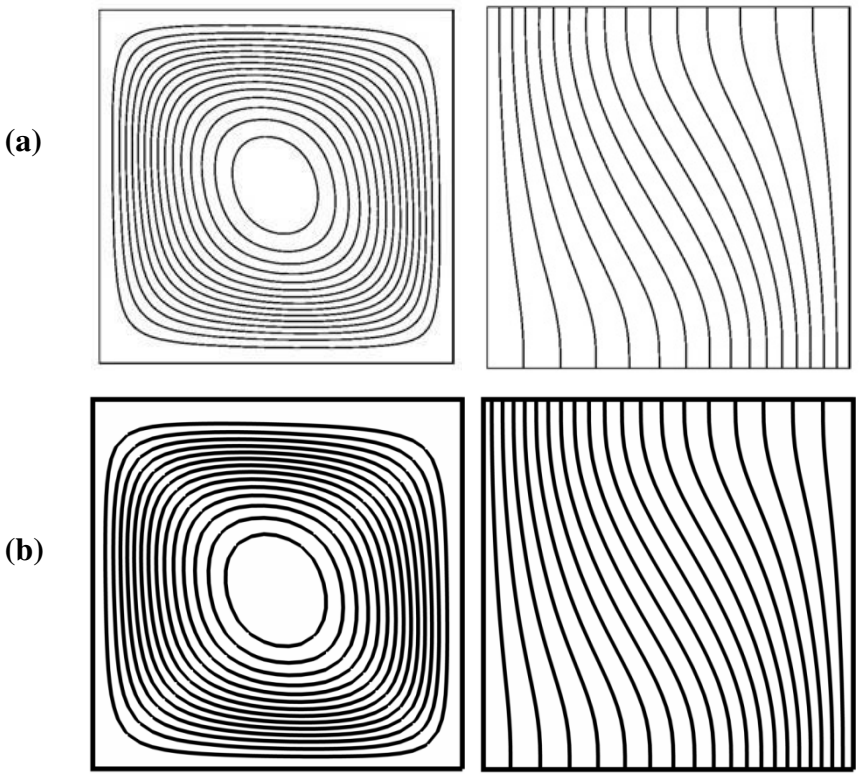

Fig. 3. Comparison of the streamlines and isotherms between (a) numerical results by Pirmohammadi and Ghassemi [13] and (b) the present results (Ra = 7000, Ha = 25)

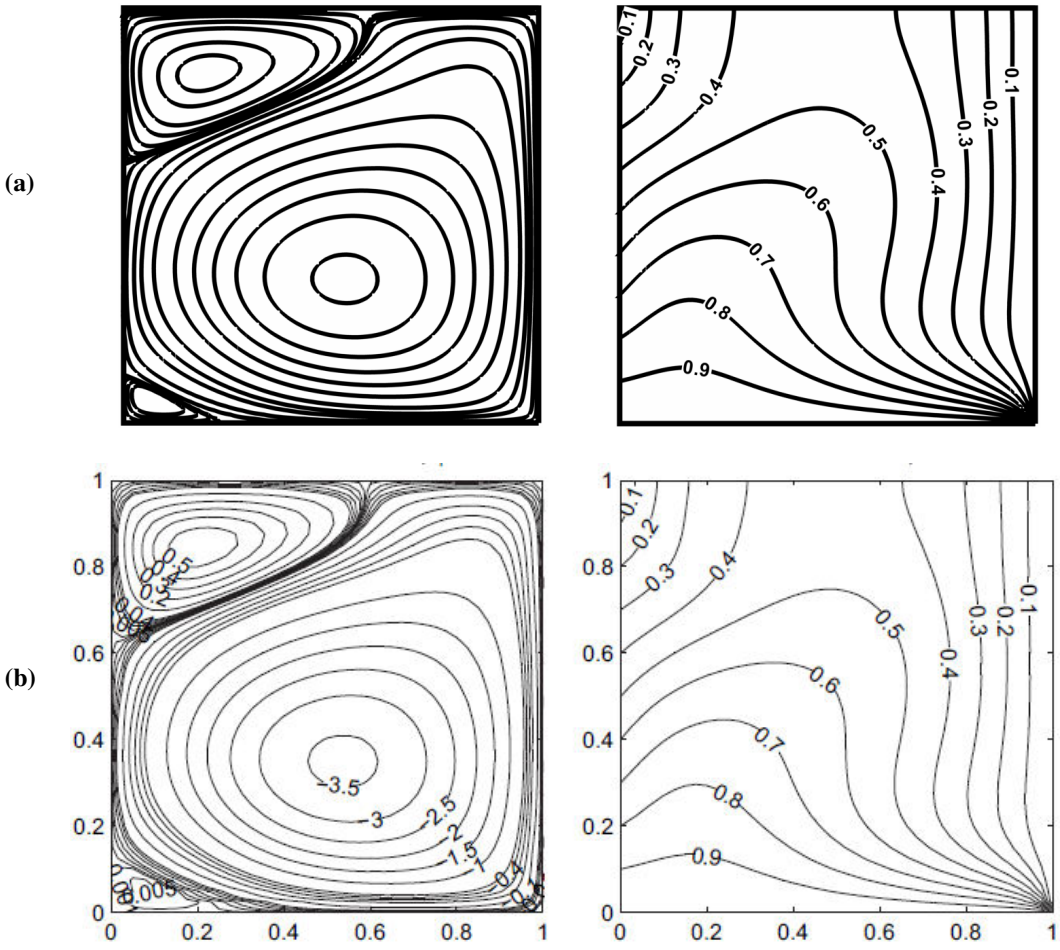

Fig. 4. Comparison of the streamlines and isotherms for natural convection at Ra=10^5 and Ha = 50 between (a) the present results and (b) numerical results by Sathiyamoorthy and Chamkha [14]

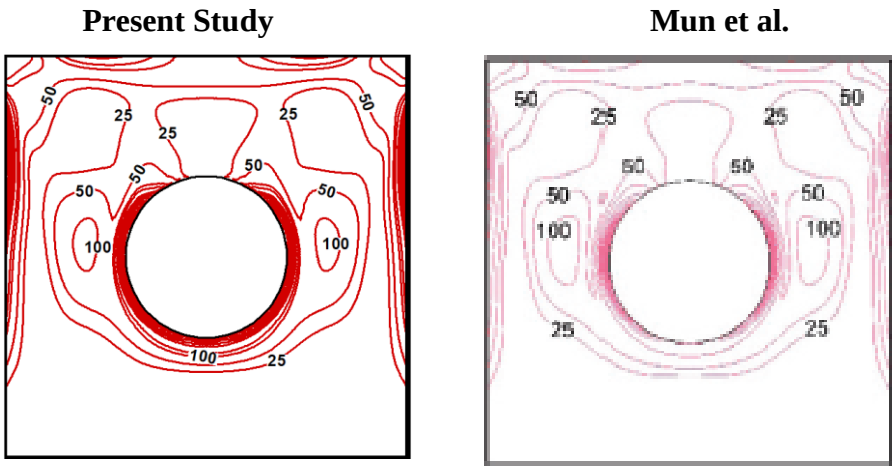

Fig. 5. The comparison of the total entropy generation at Ra = 10^5 and Pr = 0.71 between present study and Mun et al. [50]

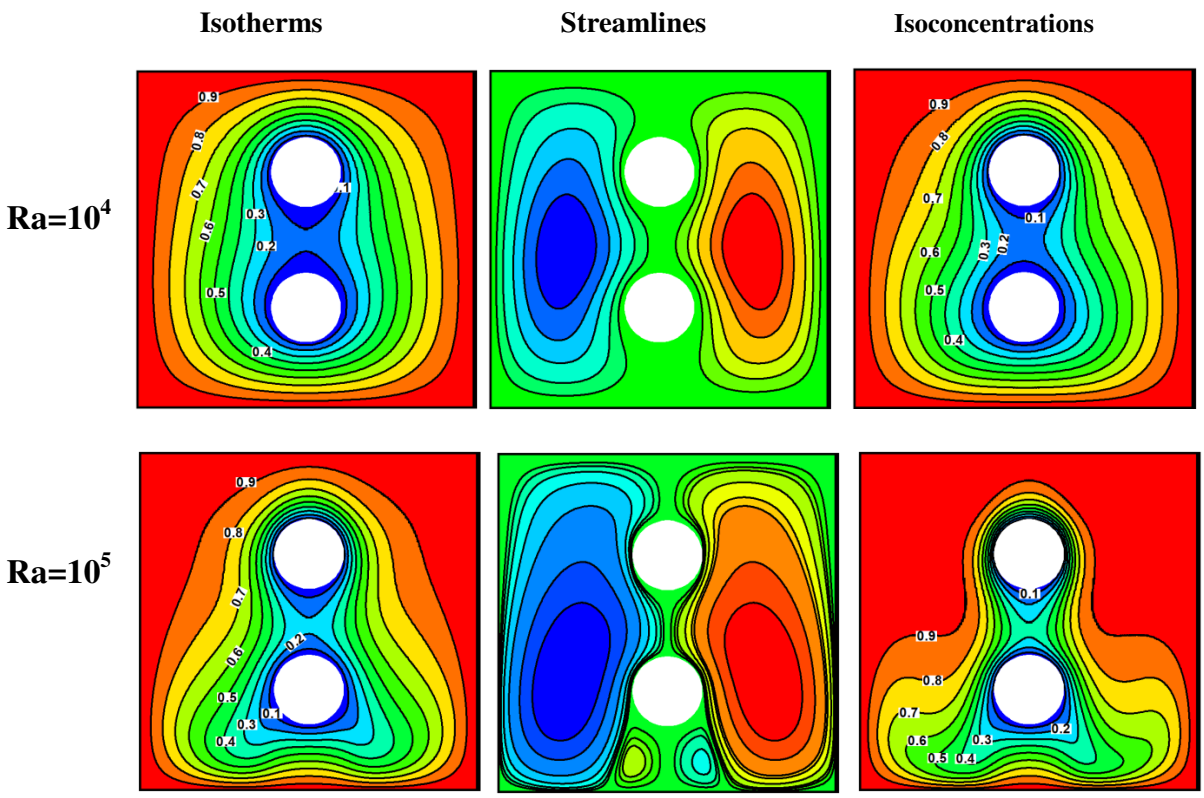

Fig. 6. Comparison of the isotherms, streamlines, and isoconcentrations for different Rayleigh numbers at Ha = 15, N = 0.1, and n = 0.2

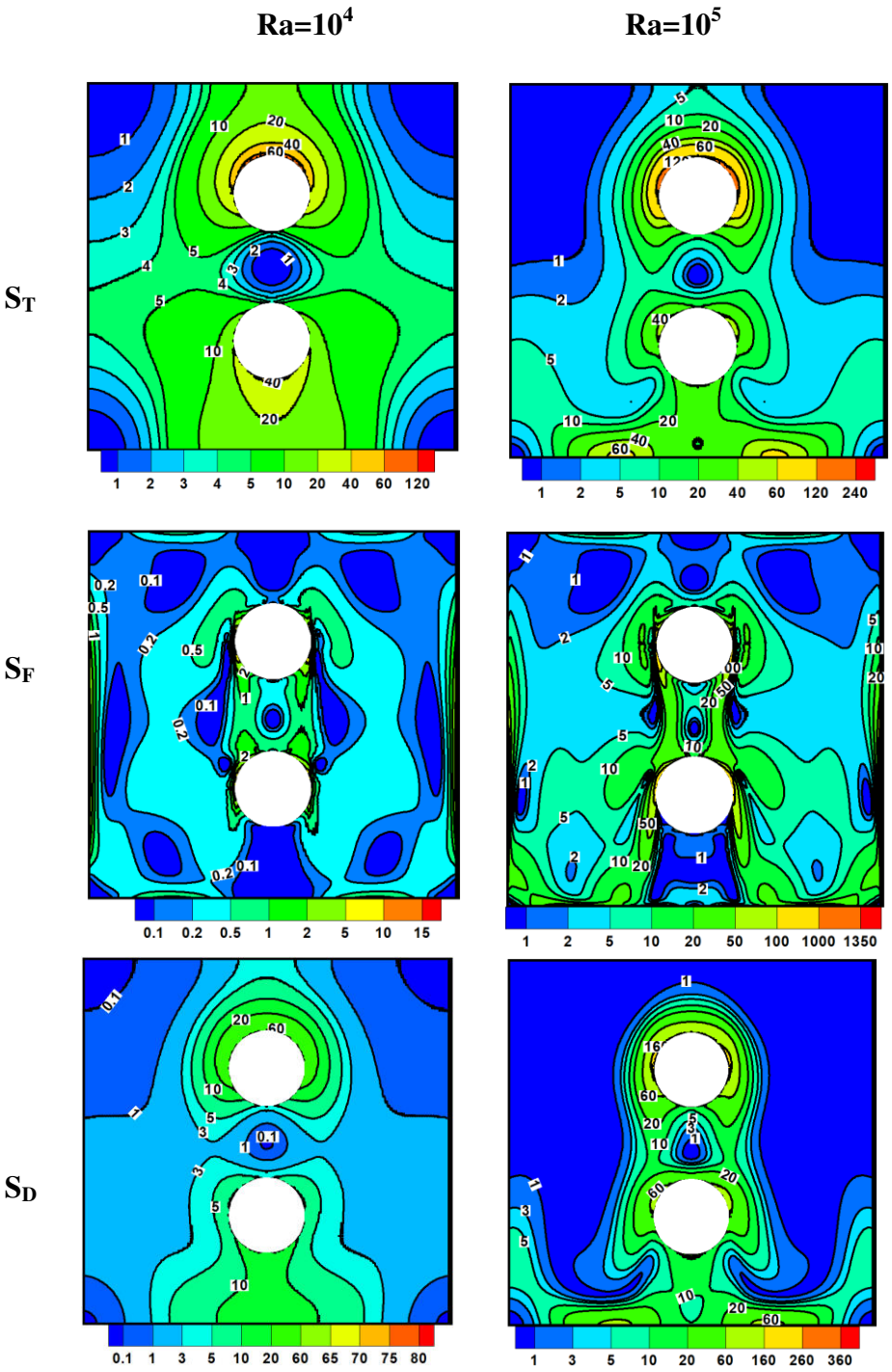

Fig. 7. Contours of the local entropy generations due to heat transfer (S_T), fluid friction (S_F), and mass transfer (S_D) at Ha = 15, n = 0.2, and N = 0.1

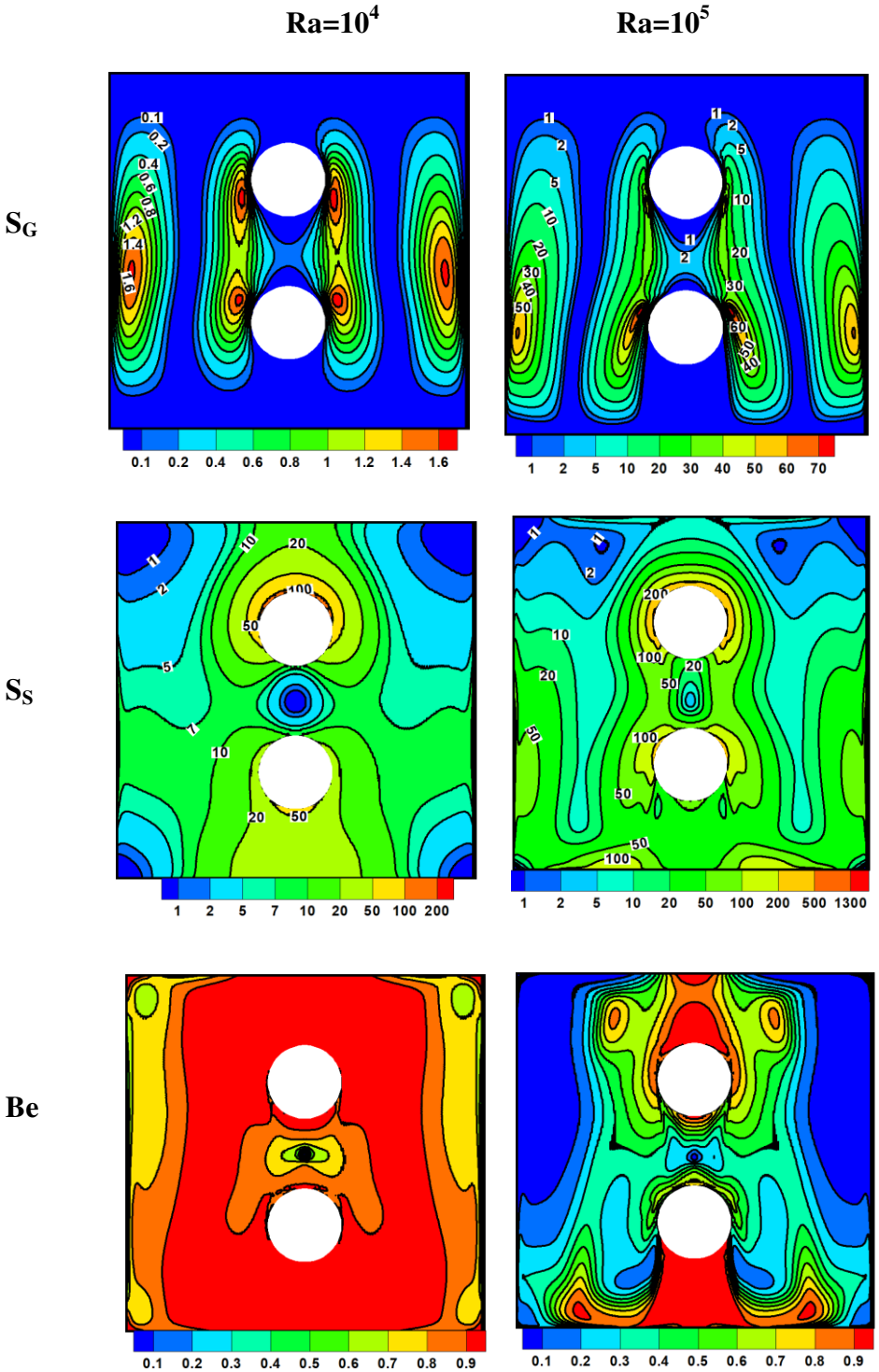

Fig. 8. Contours of the local entropy generations due to magnetic field (S_G), summation entropy generation (S_S), and the local Bejan number (Be) for different Rayleigh numbers at Ha = 15, n = 0.2, and N = 0.1

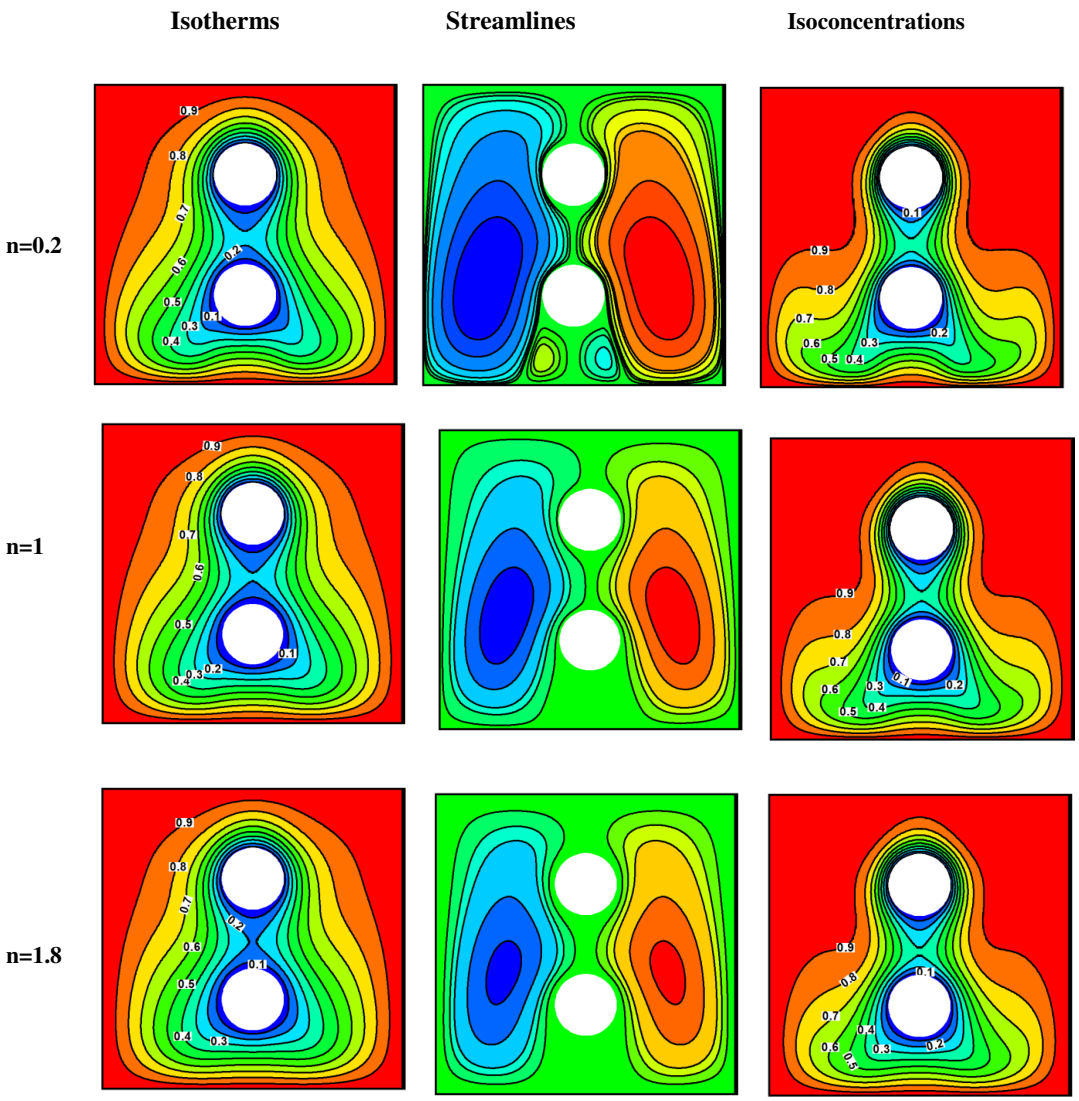

Fig. 9. Comparison of the isotherms, streamlines, and isoconcentrations for different power-law indexes at Ha=15, N = 0.1, Ra = 10^5

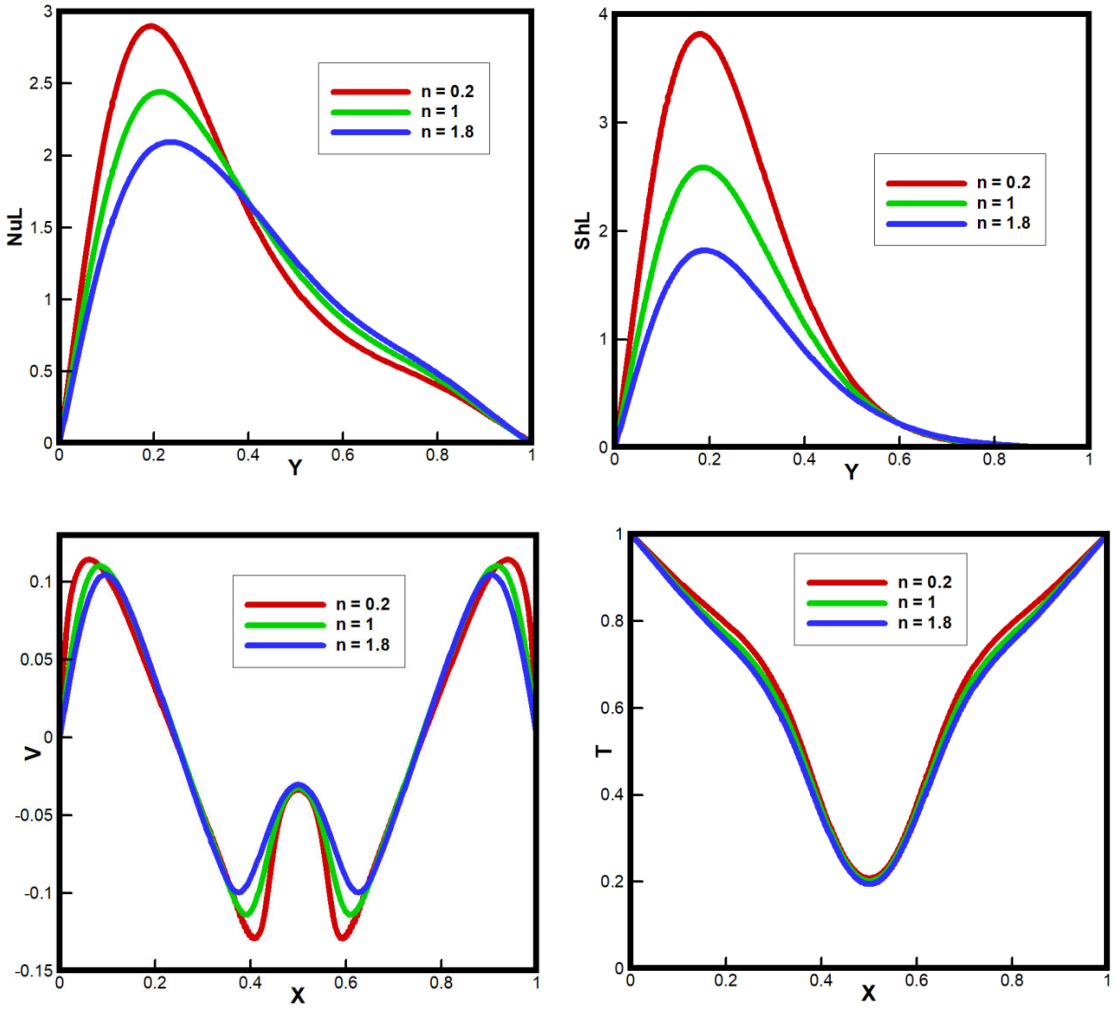

Fig. 10. Comparisons of local Nusselt and Sherwood numbers on the left hot wall, velocity and temperature distributions in the middle of the cavity for different power-law indexes at Ha = 15, N = 0.1, Ra = 10^5

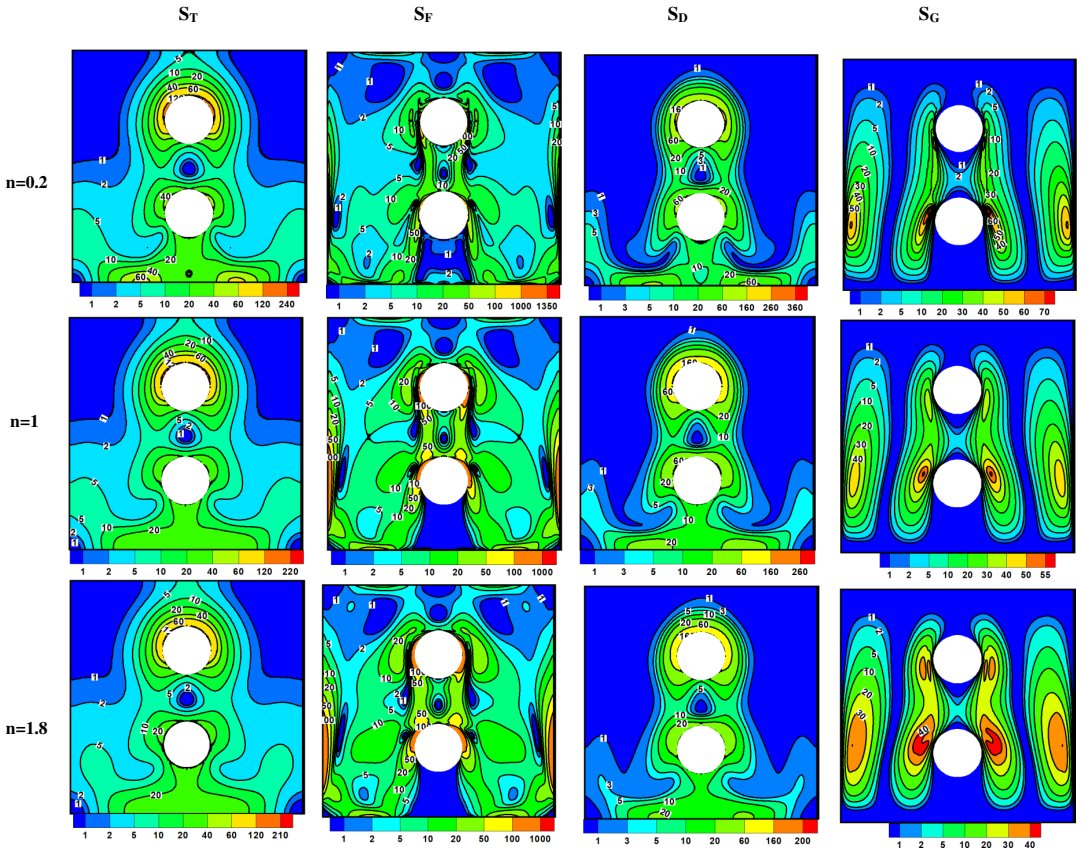

Fig. 11. Contours of the local entropy generations due to heat transfer (S_T), fluid friction (S_F), mass transfer (S_D), magnetic field (S_G) for different power-law indexes at Ra = 10^5, Ha = 15, N = 0.1

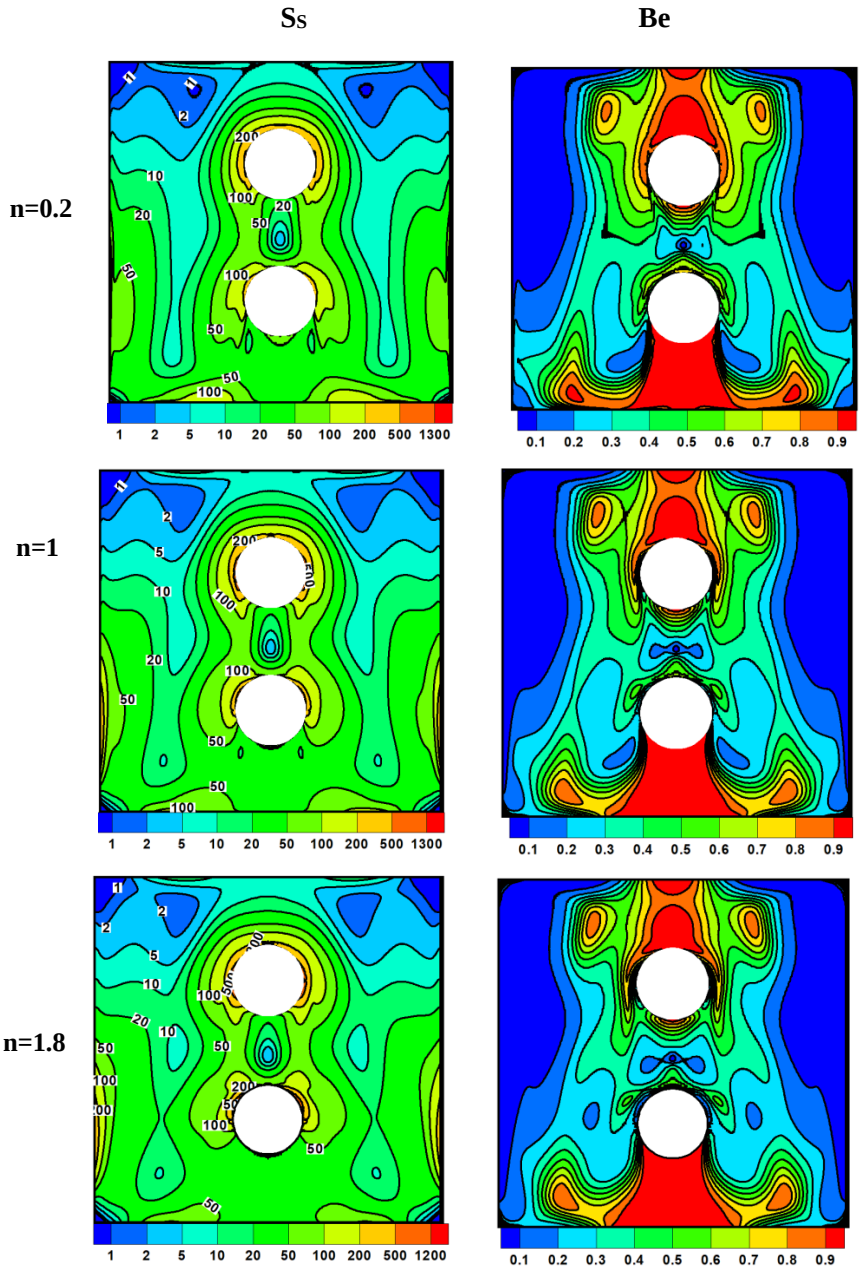

Fig. 12. Contours of the local entropy due to the summation entropy generation (S_S), and the local Bejan number (Be) for different power-law indexes at Ra = 10^5, Ha = 15, N = 0.1

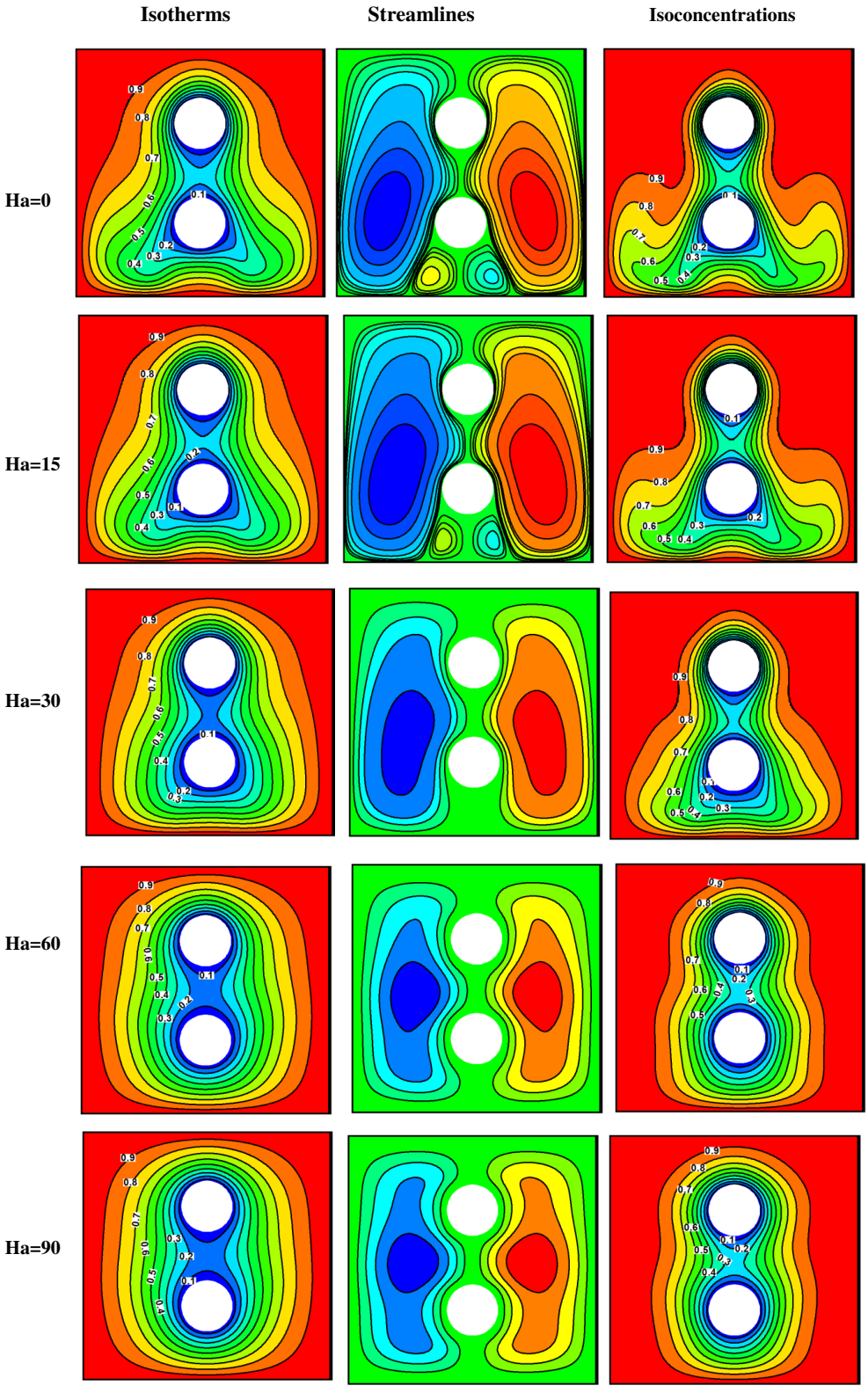

Fig. 13. Comparison of the isotherms, streamlines, and isoconcentrations for different Hartmann numbers at n=0.2, N = 0.1, Ra = 10^5

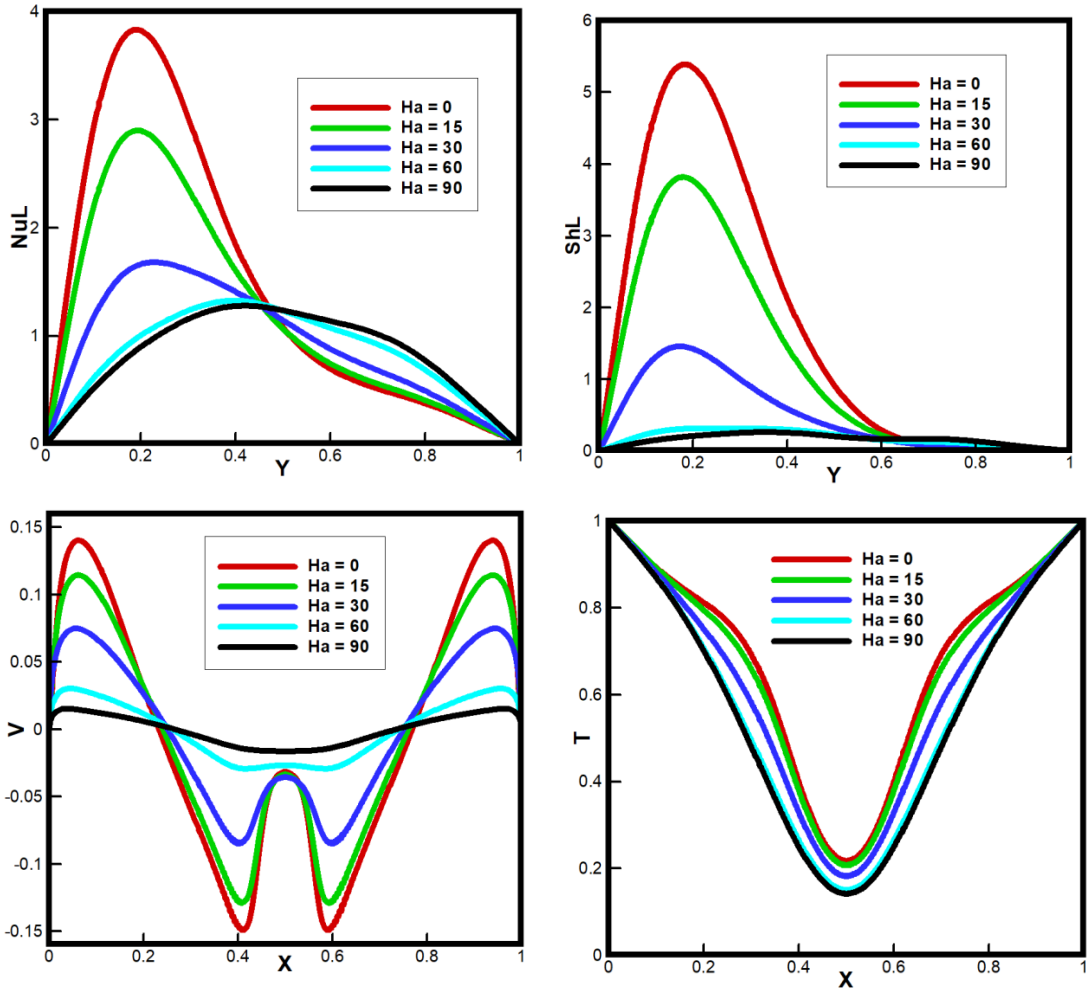

Fig. 14. Comparisons of local Nusselt and Sherwood numbers on the left hot wall, velocity and temperature distributions in the middle of the cavity for different Hartmann numbers at n = 0.2, N = 0.1, Ra = 10^5

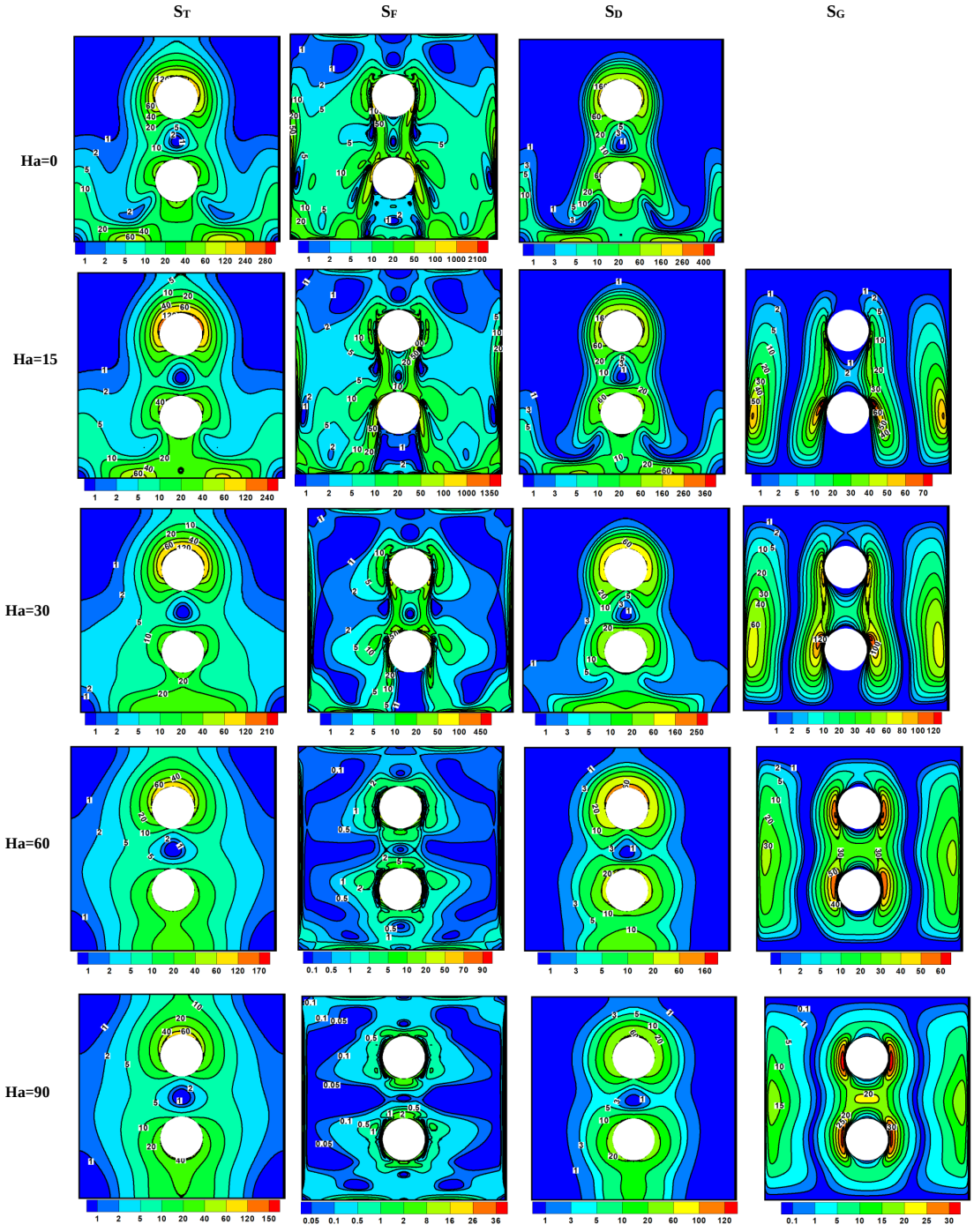

Fig. 15. Contours of the local entropy generations due to heat transfer (S_T), fluid friction (S_F), magnetic field (S_G), and mass transfer (S_D) for different Hartmann numbers at Ra = 10^5, n = 0.2, N = 0.1

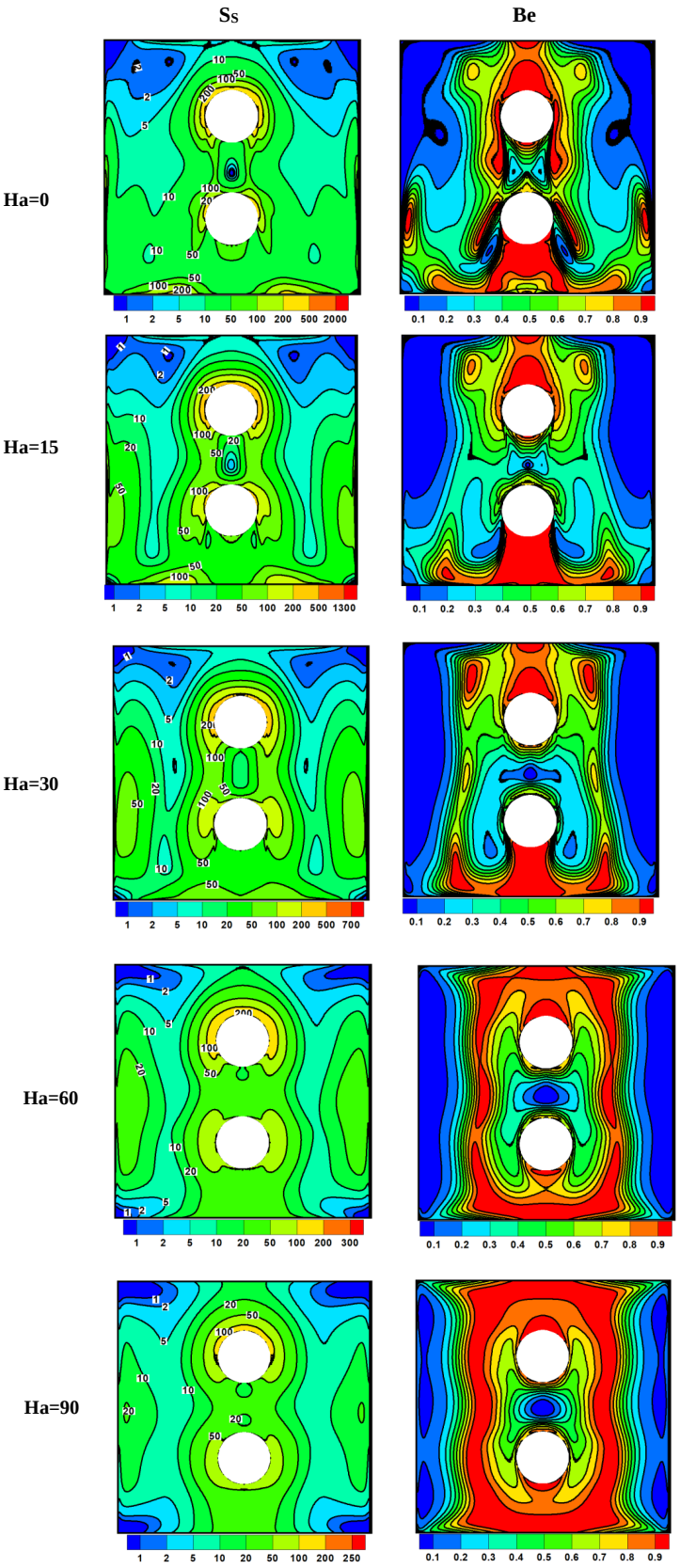

Fig. 16. Contours of the local entropy due to the summation entropy generation (S_S), and the local Bejan number (Be) for different Hartmann numbers at Ra = 10^5, n = 0.2, N = 0.1

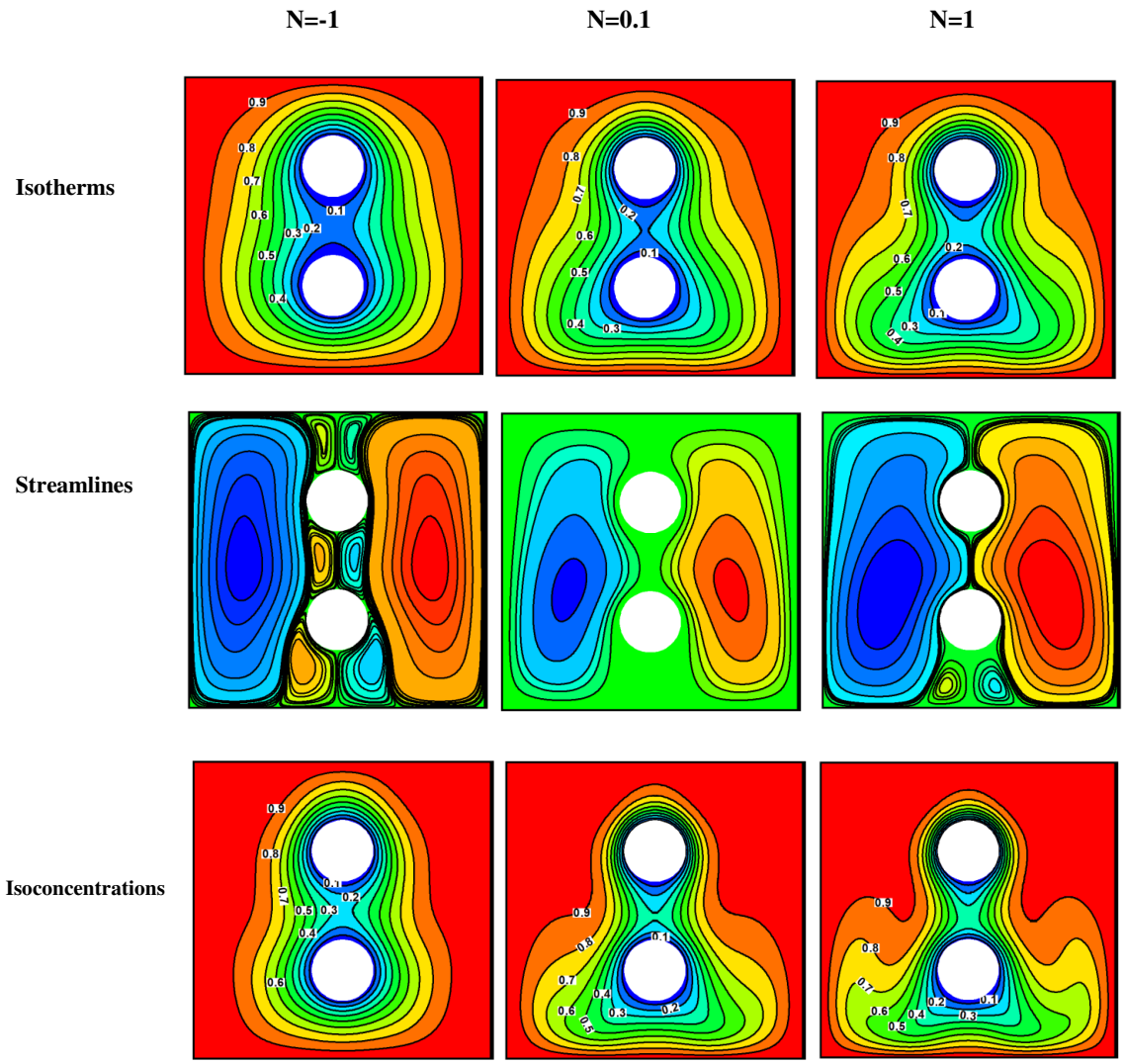

Fig. 17. Comparison of the isotherms, streamlines, and isoconcentrations for different Buoyancy ratios at Ra = 10^5, n = 1.8, Ha = 15

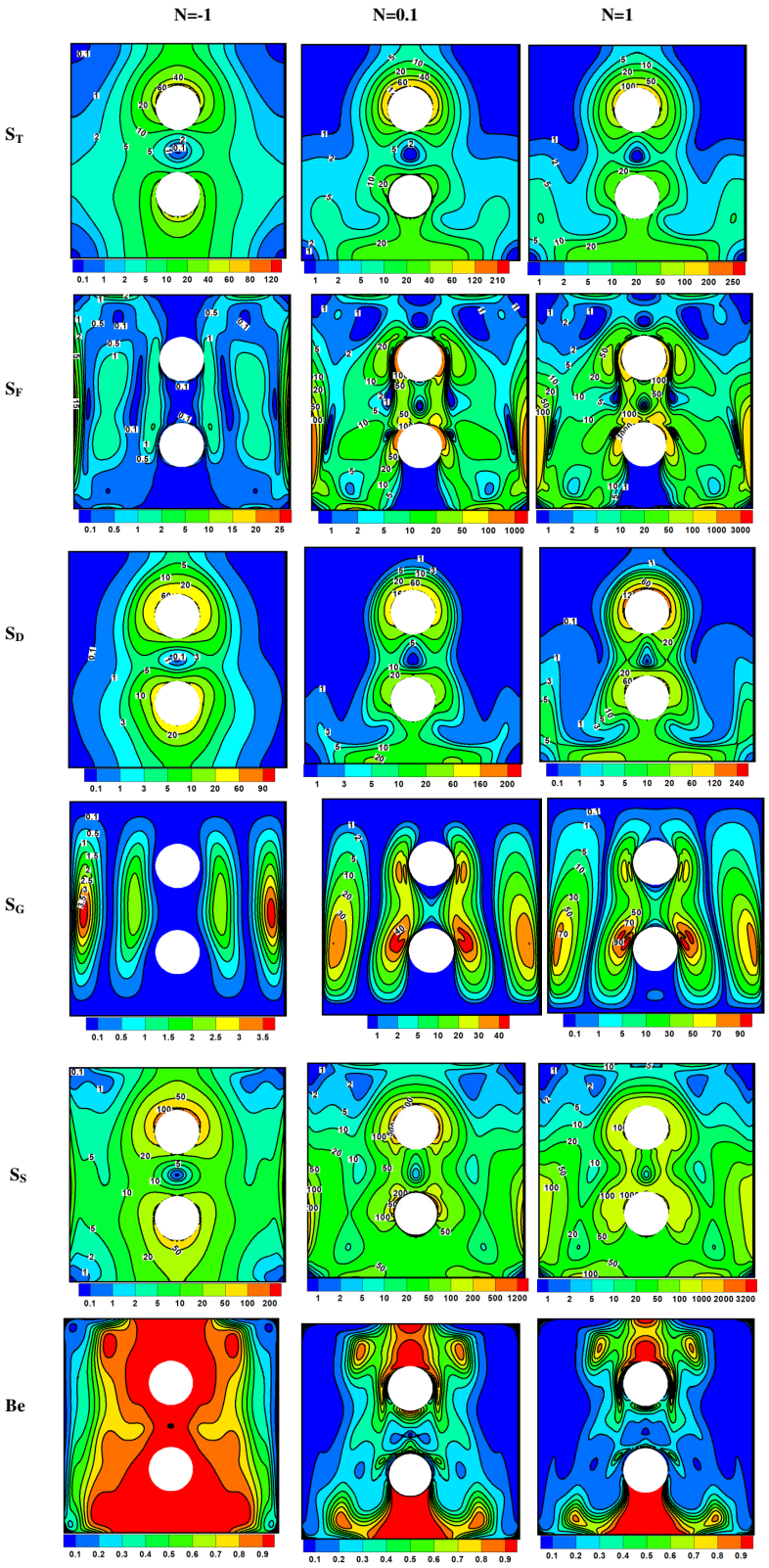

Fig. 18. Effects of the Buoyancy ratio (N) on the local entropy generations due to heat transfer (S_T), fluid friction (S_F), mass transfer (S_D), summation entropy generation (S_S), and the local Bejan number (Be) at n = 1.8, Ra = 10^5, Ha = 15